Materials Science & Engineering A 888 (2023) 145799

Contents lists available at ScienceDirect

Materials Science & Engineering A

journal homepage: www.elsevier.com/locate/msea

Influence of process and heat input on the microstructure and mechanical properties in wire arc additive manufacturing of hot work tool steels

Florian Pixner [a,*], Ricardo Buzolin [a], Fernando Warchomicka [a], Mária Dománková [b], Mária Čaplovičová [c], Florian Riedlsperger [a,d], Sebastian Fritsche [a], Marta Orłowska [e], Josef Domitner [a], Michael Lasnik [f], Norbert Enzinger [a]

[a] Institute of Materials Science, Joining and Forming, Graz University of Technology, Kopernikusgasse 24, 8010, Graz, Austria
[b] Institute of Materials Science, Faculty of Materials Science and Technology in Trnava, Slovak University of Technology in Bratislava, Bottova 25, 917 24, Trnava, Slovakia
[c] Centre for Nanodiagnostic, Faculty of Materials Science and Technology in Trnava, Slovak University of Technology in Bratislava, Vazovova 5, 812 43, Bratislava, Slovakia
[d] Institute of Engineering Materials- Metals and Alloys, Johannes Kepler University Linz, Altenberger Straße 69, A-4040, Linz, Austria
[e] Faculty of Mechanical Engineering, Military University of Technology, Kaliskiego 2, 00-908, Warsaw, Poland
[f] Voestalpine BÖHLER Aerospace GmbH & Co KG, Mariazeller Straße 25, A-8605, Kapfenberg, Austria

ARTICLE INFO

Keywords:
Wire arc additive manufacturing
Cold metal transfer
Gas metal arc welding
Hot work tool steel
Microstructure
Mechanical properties

ABSTRACT

The present study demonstrates the suitability of wire arc additive manufacturing (AM) for hot work tool steel processing. Different arc welding techniques and energy inputs were applied and systematically compared to determine the deposition characteristics, microstructure and mechanical properties. All AM deposits show a sound visual appearance and full density without macroscopic imperfections, i.e. cracking. By adhering to a predefined interpass strategy, the cold metal transfer process can be used to achieve higher weld beads with lower dilution and faster build-up rates than the metal active gas process. The microstructure of the AM parts is comparable for all process configurations and consists of an α/α′-matrix with a finely dispersed vermicular and polygonal δ-ferrite network; no notable amount of retained austenite could be measured, but it could be observed by transmission electron microscopy embedded within the laths. Intensive precipitation of multiple molybdenum-based precipitates is observed along the interface matrix to δ-ferrite. In contrast, iron-based precipitates are predominantly found inside and at the boundaries of the laths of the matrix. Similarities are also evident in the mechanical properties, resulting in an average hardness of 380–390 HV1 and absorbed impact energy of 10–12 J at room temperature. High yield strength values of 1000–1100 MPa and ultimate tensile strength of 1200–1400 MPa were obtained. No significant differences in the measured mechanical properties could be noted regarding the specimen orientation, indicating the isotropy of the properties.

1. Introduction

In service, tools are exposed to complex thermomechanical loading conditions and place high demands on material performance, e.g. high wear resistance, extended service lifetimes and the possibility of economical repair, including welding [1,2]. A variety of hot work tool steels have been developed that combine the characteristics of strength, wear resistance, and toughness under normal service conditions [3,4]. In addition, the materials should be resistant to mechanical and thermal-induced cracking as well as plastic deformation [2]. The most widespread grades are AISI H11 (1.2343/X38CrMoV5-1) and H13 (1.2344/X40CrMoV5-1), mainly used for the manufacturing of conventional forging dies, injection molds and dies for presses.

Even though these medium-carbon martensitic chromium hot work tool steels (e.g. AISI H11, H13) are widely applied in tool industry, processing them by additive manufacturing remains challenging. Laser Powder Bed Fusion (L-PBF) [5–12] and Laser Metal Deposition (LMD) [13–17], i.e. powder-based processes, are mainly used to process such tool steels. The material shows an increased susceptibility to cracking due to its carbon content and the complex thermal cycling/residual

* Corresponding author.
E-mail address: florian.pixner@tugraz.at (F. Pixner).

https://doi.org/10.1016/j.msea.2023.145799
Received 22 December 2022; Received in revised form 10 October 2023; Accepted 11 October 2023
Available online 12 October 2023

stresses that occur in powder-based processes, limiting its application. Regarding L-PBF, the susceptibility to cracking can be reduced by preheating the build platform to a higher temperature [18], but cracking can still occur. L-PBF processes are considered as leading technologies when producing complex geometries combined with good surface qualities. However, the powder size in the micrometer range and the limitations imposed by the working chamber dimension restrict the achievable deposition rates and part sizes [19].

Wire-based Arc Additive Manufacturing (WAAM) has high innovation potential here, and particularly in tool manufacturing. This form of AM can be utilized to restore the geometries of damaged structures as well as to manufacture larger tool inserts that have customized geometric, technological, and metallurgical properties. Such hybrid manufacturing processes (i.e. additive manufacturing of required geometries on conventionally subtractively manufactured parts) are only limited feasible for L-PBF, and direct energy deposition (DED) processes like WAAM are more eligible. WAAM expands the established repair- and AM techniques, offering a new strategy for restoring a worn and cracked near-net-shape volume on a larger scale. However, very little information is available about the WAAM of hot work tool steel grades. The availability of suitable filler metals is highly limited, and processing certain tool steel grades presents significant challenges. These grades are conditionally weldable in the states: 1) annealed, 2) hardened as well as in 3) tempered, and material needs to be preheated to a sufficient level above the martensite starting temperature (Ms). During the deposition process, the interpass temperature should remain between 325 °C and 475 °C [20]. Suitable filler metals for processing chromium hot work tool steels are rare, and the X10CrMo6-3 grade is one of the few filler metals that is considered to meet manufacturers' guidelines [20,21]. This grade is characterized by its improved wear resistance combined with sufficient toughness. Casati et al. [6] found that such low-carbon composition of hot work tool steel is of major interest for AM, in particular for printing parts with more complex geometry. These grades are expected to provide a better toughness combined with a higher resistance to residual stresses- and process related defects. Stockinger et al. [22] and Pixner et al. [23] demonstrated that these lean carbon grades could also be used for WAAM and for fabricating hybrid structures or structural parts with AISI H11/13.

In WAAM, an electric arc is used to melt the filler wire material. Different processes can be used for WAAM [24], such as gas metal arc welding (GMAW) [25,26], cold metal transfer (CMT) [25,27], gas tungsten arc welding (GTAW) [28–31] and plasma welding [32–34]. While the filler material is introduced separately from the energy in the plasma and GTAW processes, the energy and material introduction are coupled in the CMT and GMAW processes. The respective material input/build-up rate is directly proportional to the energy input. Since volumetric AM components are usually built up over several hours and are subjected to self-tempering, the heat management and thus energy input play a crucial role. Thermal management is a critical factor in WAAM for maintaining an economic process and mitigating heat accumulation, both of which can help to overcome the limitations of the deposition cycle, improve geometric accuracy, and ensure the anisotropy of mechanical properties [35,36]. Especially for thermally sensitive materials with interpass temperature requirements (e.g., HSLA [37]) or heat treatments (e.g. hot work tool steel [38,39]), the temperature distribution, as well as material and energy input, are critical factores for the formation of the microstructure and the associated mechanical properties of the part. The selection of the arc welding technique, process parameters, and build strategy are important for thermal management as they allow to control the heat input and, consequently, the characteristics of the parts built.

CMT and GMAW are widely applied in WAAM and are characterized by their different process characteristics. GMAW is a welding process offering a great potential for producing large-scale parts due to its high energy efficiency and deposition rates [24]. However, GMAW is limited to a minimum wall thickness and surface finish due to the relatively large melt pool, heat input, and limited arc stability [24,40–42]. By applying CMT welding, a modified short circuit arc process developed by *Fronius* [43], these constraints can be overcome by reducing the burning period of the arc, i.e. reducing the energy input and reversing the wire electrode back and forth [44–46]. Exceptional arc stability, drop-by-drop controlled material deposition, low heat input, nearly spatter-free application, and high process tolerance are typical CMT process characteristics. Therefore, CMT has been selected as a promising arc-based AM method [27,47,48]. The successful application of CMT for the WAAM of various materials such as steels [41,46,49], titanium- [50,51], nickel-based [52–54], magnesium- [55–57], and aluminium alloys [58,59] has already been demonstrated. In general, the average deposition rate is lower in CMT, although the process is highly suitable for producing thin-walled components with challenging near-net shapes and geometric features [24].

The literature on the WAAM of hot work tool steels is limited. In addition, information about the arc welding techniques, heat input, microstructure development, and mechanical properties is lacking, because specific hot work tool steel grades remain challenging to investigate. This study was carried out to demonstrate the suitability of WAAM for building voluminous AM parts that can be used to restore hot work tool steel components for use in the tooling industry. A systematic comparison was made between different arc welding techniques and energy inputs, and the influence on the resulting microstructure and associated properties was investigated.

2. Materials and methods

2.1. Materials

The substrate used was AISI H11 (1.2343, X38CrMoV5-1), a chromium martensitic hot work tool steel, with a thickness of 35 mm. The substrate was quality heat treated, namely quenched and tempered, to a hardness of 380–420 HB (which corresponds to approx. 400–440 HV). A suitable low-carbon solid filler wire X10CrMo6-3 with increased chromium and molybdenum content was used to deposit the AM structures on the substrate. The diameter of the filler wire was Ø 1.2 mm, and the filler wire material as well as the wire diameter were kept constant throughout the study, i.e. for both CMT and MAG processes. The nominal chemical compositions of the materials are listed in Table 1.

High-alloyed steels and the corresponding microstructure are described by the Schaeffler diagram or variants like WRC-1992 and DeLong, using the chromium Cr_{eq} and nickel Ni_{eq} equivalents. In dependence on the calculated Cr_{eq} and Ni_{eq}, a certain range with a specific microstructure is observed, enabling a phase prediction to be made based on the Cr_{eq} and Ni_{eq} of the chemical composition of the built part. The Cr_{eq} and Ni_{eq} coordinates for materials used are calculated as follows, where the respective coefficients represent the relative contributions of each element to austenitic or ferritic stability [62]:

$$Cr_{eq} = \%Cr + \%Mo + 1.5 \times \%Si + 0.5 \times \%Nb + 2.0 \times \%Ti \quad \text{Equation 1}$$

$$Ni_{eq} = \%Ni + 30 \times \%C + 0.5 \times Mn + 30 \times \%N \quad \text{Equation 2}$$

The derived Cr_{eq} and Ni_{eq} values for the nominal chemical composition of the solid wire and the base material are summarized in Table 1; in Fig. 1 the corresponding positions are marked in the Schaeffler diagram. For the base material, the Cr_{eq} and Ni_{eq} are 7.85% and 11.60%, and for the solid wire, 10.40% and 3.30%, respectively.

2.2. Welding equipment

The shielding gas M21-ArC-18 (ISO 14175:2008 18 vol% CO2 and 82 vol% argon) for CMT in standard mode and M20-ArC8 (ISO 14175:2008 8 vol% CO_2 and 92 vol% argon) for pulsed MAG welding was used. The gas flow rate of the shielding gas was 15 l/min. The CMT system used is consisting of a Fronius TPS 400i welding power source, a

Table 1
Nominal chemical composition in wt.% of the substrate AISI H11 (1.2343, X38CrMo5-1) and filler wire X10CrMo6-3 [60,61].

Material	C	Cr	Mo	Mn	V	Si	Fe	Cr_{eq}	Ni_{eq}
Substrate H11	0.38	5.20	1.30	0.40	0.45	0.90	bal.	7.85	11.60
Solid Wire X10CrMo6-3	0.10	6.50	3.30	0.60	–	0.40	bal.	10.40	3.30

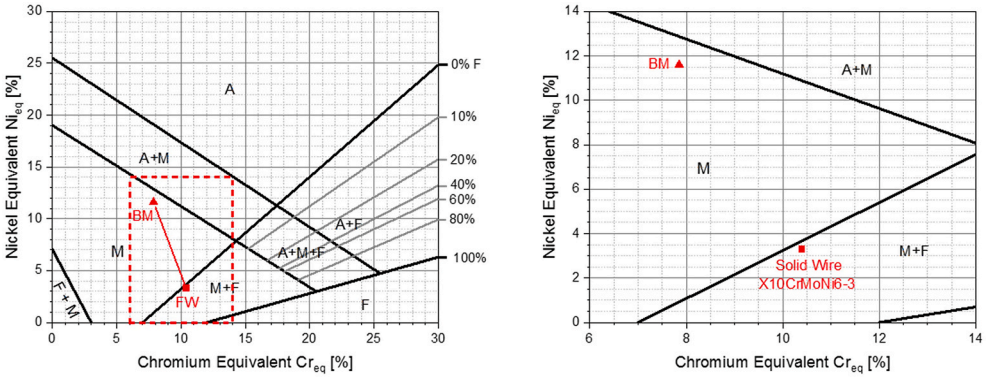

Fig. 1. (a) Schaeffler diagram and (b) detail of a specific area of interest with the materials used marked in red; FW.: filler wire, BM.: base metal, F.: ferrite, A.: austenite, M.: martensite. (For interpretation of the references to colour in this figure legend, the reader is referred to the Web version of this article.)

WF 60i Robacta Drive CMT push-pull torch unit, and a wire buffer. The welding characteristic MAG Puls-Synergic was used for MAG, a variant of pulsed MAG welding. The motion control system consisted of an ABB IRB 140 six-axis articulated robot, an ABB IRBP A positioner, and the IRC5 control system.

2.3. Experimental

The optimized parameters for the present study are listed in Table 2; these were selected based on a previously conducted design of experiments (DoE) using a central composite design (CCD) (shown in the supplementary data). For the CCD, single-track welds were deposited on the substrate preheated to 400 °C (above Ms temperature of AISI H11) and the following parameters were varied: 1) welding current from 178 to 262 A for CMT and 165–225 A for MAG and 2) welding speed from 0.65 to 1.35 cm/s. The objective of the CCD was to determine process parameters (e.g. welding current) for each process that would provide similar material input (i.e. wire feed) for the respective processes. To ensure the comparability of the two processes, two identical material inputs were chosen for the CMT and MAG processes: a low energy input of 5.40 m/min and a high energy input of 7.20 m/min. The material input serves as an important indicator in AM and can be set directly as an input parameter (since it correlates with welding current) in the power source, making it more suitable as a reference than the energy input. The energy input is derived from several welding parameters, which may be subject to change. Due to the intrinsic process characteristics of the two different arc techniques, a different energy input was introduced even though the material input was comparable. The power and energy input per unit length was derived from the welding parameters and is listed in Table 2.

The AM structures were additively manufactured using different processes and energy inputs and subsequently characterized to determine their microstructural and mechanical properties. The deposition process was performed on an AISI H11 substrate preheated to 400 °C. The required minimum dimensions of the volumetric structures for sampling and multiaxial mechanical testing are 70 × 20 × 120 mm (Fig. 2b). The structures were fabricated in layers, with each layer consisting of three adjacent weld beads with an axial offset η of 65% of the weld bead (Fig. 2a). The value for the axis offset/overlap distance and the selected weld sequence were chosen based on literature (axis offset [22,46,63,64], weld sequence [22,46,65]). The interlayer temperature was manually monitored using type K thermocouples with a

Table 2
Selected process parameter configuration for WAAM of hot work tool steel via cold metal transfer (CMT) and metal active gas (MAG) welding.

Attribute	Variable	Unit	Values			
			CMT		MAG	
			Low Energy	High Energy	Low Energy	High Energy
Welding current	I_{weld}	A	190	250	165	215
Welding voltage	U_{weld}	V	15.6	16.7	23.2	24.2
Power input	P	kW	2.96	4.18	3.83	5.20
Energy input	E	kJ/cm	3.95	5.57	5.10	6.93
Wire feed rate	V_{wire}	m/min	5.40	7.20	5.40	7.20
Welding speed	V_{weld}	cm/sec	0.75			
Electrode stick-out	-	mm	15			
Work angle	-	°	0			
Travel angle	-	°	0			
Gas flow rate	-	l/min	15			
Arc length correction	-	–	None			
Arc dynamic correction	-	–	None			

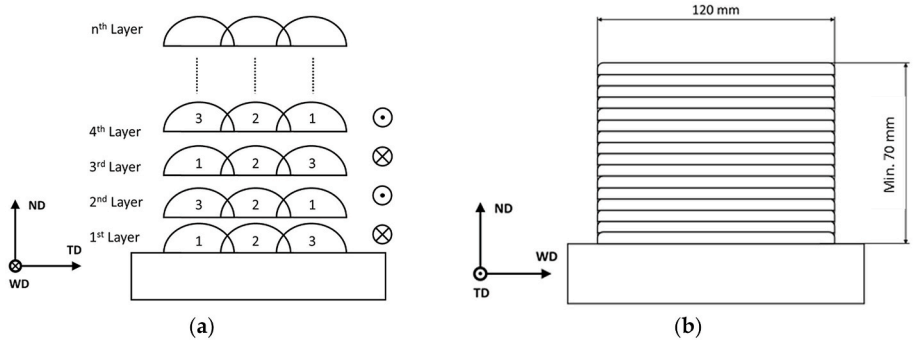

Fig. 2. (a) Schematic illustration of the selected welding sequence; (b) side view of the AM structure with the required minimum dimensions [23].

diameter of Ø 0.2 mm. After each deposited layer, the deposition process was paused, the interlayer temperature was then measured manually, and the subsequent layer was deposited on top of the previous one once the interlayer temperature was within a range of 350–400 °C, which is approximately the Ms temperature. The final number of layers deposited to achieve the desired height and the average build-up rates depend on the selected welding parameters and are discussed in the following sections.

2.4. Characterization

The microstructure and mechanical properties of the fabricated AM structures were characterized. Different sample orientations (i.e. horizontally/vertically oriented) were taken into account for the mechanical characterization in order to examine the mechanical anisotropy. The properties of the AM structures were evaluated in terms of the applied process, energy input, and orientation. The mechanical properties: 1) hardness, 2) Charpy V-notch impact toughness, and 3) tensile strength were determined. For statistical validation of the results, three specimens were examined for each configuration's tensile and Charpy-V notch test results, and the mean values and standard deviations were derived. The microstructures formed were characterized by using digital microscopy (DM), scanning electron microscopy (SEM) with electron backscatter diffraction (EBSD) and energy-dispersive X-ray spectroscopy (EDXS), X-ray diffraction (XRD), and transmission electron microscopy (TEM). In addition, the chemical composition of the AM structures was measured by using optical emission spectroscopy (OES).

2.4.1. Microstructural characterization

Digital microscopy was performed using a Keyence VHX-6000. The cross-sections (ND-TD plane) were hot mounted, ground to #2000 grit SiC paper, and polished with a silicon oxide polishing suspension (OPS). The cross-sections were wet etched for 20 s with a modified Lichtenegger-Bloech etchant composed of 100 ml distilled water, 0.75 g ammonium hydrogen difluoride, and 0.9 g potassium disulfate.

Cross-sections were similarly prepared for scanning electron microscopy, without wet etching for EBSD and EDXS studies and with 5% Nital etchant (solution of HNO_3 in C_2H_6O) for backscattered electrons (BSE). The SEM investigation was performed using a TESCAN Mira3 microscope equipped with a Super Octane energy-dispersive X-ray spectroscopy, a Hikari camera, and an APEX software package for the EBSD and EDXS analysis. The EDXS analysis was carried out using an acceleration voltage of 20 kV, a working distance of 15 mm, and a spot size of 60 nm. EBSD measurements were performed using an acceleration voltage of 25 kV, a working distance of 20 mm, and a spot size of 60 nm over an area of 100 µm × 100 µm, with a step size of 0.16 µm. The generally accepted transition angle between LAGB and HAGB of 15° in the case of an ideal arrangement of dislocations [66] was used to define a high-angle grain boundary. Using the OIM Analysis v.8.6 software, a minimum grain size of 1 µm was chosen to verify that each grain consisted of at least five measured pixels. The confidence index was standardized. The EBSD data were cleaned, considering a minimum confidence index of 0.1 correlated to the neighbouring grains.

X-ray diffraction (XRD) was carried out on samples' ND-TD plane with a Rigaku MiniFlex600. XRD measurements were performed at room temperature on specimens in polished condition with a 10 × 10 mm minimum cross-sectional area.

TEM observation was performed using a JEOL 200CX microscope operating at 200 kV. Two types of samples for TEM were prepared: 1) one-stage carbon replicas to identify secondary phases/particles and 2) thin foils to identify the matrix character. Selected area electron diffraction (SAED) was used to identify the phases. Carbon extraction replicas were prepared in several steps. After grinding and polishing the samples, they were etched with solution COR (10 ml HCl + 6 ml CH_3COOH + 1g $C_6H_3N_3O_7$ + 72 ml C_2H_6O) for 5–10 s. Then, a thin layer of carbon was applied to the surface to be removed from the samples using anodic dissolution in 3% Nital (solution of HNO_3 in C_2H_6O) at a voltage of 20 V. The TEM thin foils were prepared in the twinjet electrolytic polishing equipment TENUPOL5 using a solution containing 30 vol% HNO_3 and 70 vol% CH_3OH at the temperature of −15 °C and 15 V. In addition, TEM using a JEOL JEM-ARM200CF double-corrected field emission atomic resolution analytical transmission electron microscope equipped with a JEOL JED-2300 0.98 steradian solid-angle silicon drift detector was used to perform energy-dispersive X-ray spectroscopy (TEM-EDXS) and to determine the elemental distribution and composition of the nanoscale precipitates.

2.4.2. Mechanical characterization

The hardness measurements were carried out according to the standard DIN EN ISO 6507-4: 2006-03 with an automated EMCO M1C hardness machine. Vickers (HV) indentations were made with a load of 1 kp (HV1) and a dwell time of 15 s. The spacing between adjacent indentations was 1 mm, and hardness maps were prepared for the cross-sections in the ND-TD plane with different processes and energy inputs.

Tensile tests at room temperature were carried out using a Zwick Roell ZMART PRO machine according to DIN EN ISO 6892-1 with vertically (load-direction: ND, designated fracture plane WD-TD) and horizontally (load-direction: WD, designated fracture plane ND-TD) oriented specimens extracted from the AM structures. Round specimens DIN 50125-B 6 × 30 with a gauge diameter of 6 mm, a gauge length of 30 mm and a total length of at least 60 mm were selected as specimen geometry. The specimens were initially preloaded to 200 N and then subjected to stroke-controlled loading at a 1 mm/min constant test speed until they fractured.

The sample impact toughness was determined at room temperature for the WD-TD plane (vertical orientation) and ND-TD plane (horizontal orientation), as shown in Fig. 3. Testing was performed following DIN EN ISO 148-1 using Charpy ISO V notch specimens with a dimension of 55 × 10 × 10 mm (length x width x height) and a notch depth of 2 mm. Information on specimen and notch orientation is shown in the

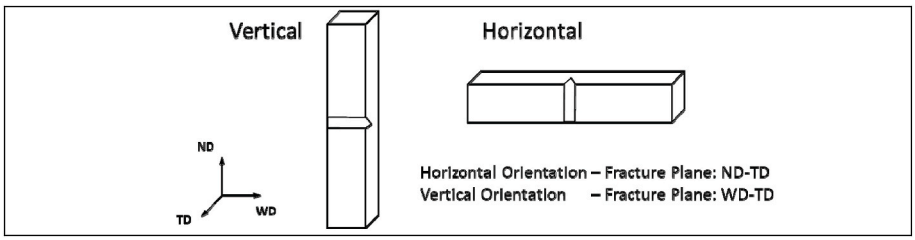

Fig. 3. Schematic illustration of the orientation of the Charpy V-notch specimen, the notch location and the intended fracture plane.

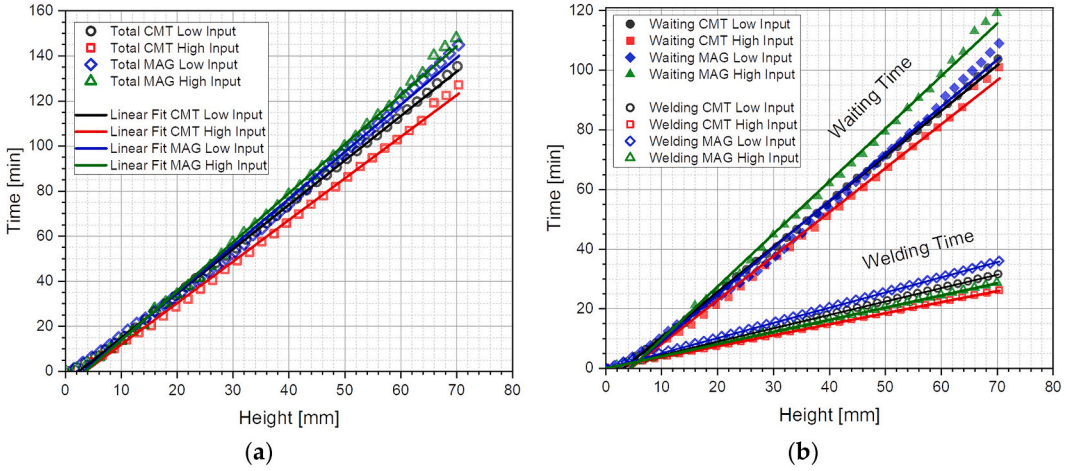

Fig. 4. (a) Build-up times and (b) associated welding and waiting times for the CMT and MAG process with different energy inputs.

schematic illustration in Fig. 3.

2.4.3. Chemical composition

Atomic absorption spectroscopy was used to determine the chemical composition of the AM structures. The extracted samples had a minimum size of 25 × 25 × 15 mm and were taken from mid-height of the structures. To ensure consistency, the sample position and orientation (ND-TD plane) for all configurations remained always the same.

2.5. Thermodynamic equilibrium calculations

Thermodynamic equilibrium calculations were carried out using the MatCalc 6.03 software, employing the steel database mc_fe_v2.060.tdb. MatCalc minimizes Gibbs energies by applying Onsager's extremum principle [67] to Calphad-based thermodynamic data (see, e.g. Ref. [67]) to identify and quantify stable phases. In this work, the nominal composition of the filler wire was numerically compared against the actual chemical composition of the AM structures. By this means, volume phase fractions were evaluated, and the effects of chemical variations on the transformation temperatures were investigated. The findings are graphically summarized in equilibrium phase diagrams.

3. Results

3.1. Material deposition

Pre-defined AM structures with a specific welding sequence (overlap distance 65%, interpass temperature 350–400 °C) and geometries (min. 70 × 20 × 120 mm) were fabricated with a defined material input (5.4 m/min ∝ theoretical deposition rate 2.8 kg/h and 7.2 m/min ∝ theoretical deposition rate 3.8 kg/h). Due to the intrinsic properties of the CMT process, the periodic retraction of the wire results in mechanical droplet detachment, which leads to a lower energy input and energy reduction of about 20% for the same material input as compared to the input in the MAG process. The nominal values of energy input for low and high wire feed rates are listed in Table 2; the energy input for low wire feed rate is 3.95 kJ/cm for CMT and 5.10 kJ/cm for MAG (i.e., 22.5% reduction), and for high wire feed rate is 5.57 kJ/cm for CMT and 6.93 kJ/cm for MAG (i.e., 19.6% reduction). In addition, the weld bead geometry also changes significantly as compared to the weld beads deposited using the MAG process; while the beads deposited using MAG tend to be wider and shallower, the beads deposited using CMT are narrower and higher. For selected parameter configurations, the average layer height was 1.8 mm and 2.2 mm for the low and high energy input CMT and 1.6 mm and 2.0 mm for the low and high energy input MAG, respectively. Consequently, fewer layers were required to achieve the desired height once the CMT process was applied, and the overall heat input could be reduced. Consequently, CMT required 39 low-energy layers and 32 high-energy layers, while MAG required 44 low-energy layers and 35 high-energy layers. This represents a reduction in the number of layers of approx. 10%. Maintaining the defined interpass strategy and build sequence, a linear growth/build-up rate ($R^2 > 0.99$) was observed for each configuration. The fastest build-up rates and build time were obtained with the CMT process (approx. > 10% faster than the

Table 3
Total build time, welding time, waiting time, and average build-up rates for the deposition of AM test structures with different welding techniques and material inputs, derived from Fig. 4.

Process	Energy Input	Build Time [min]	Welding Time [min]	Waiting Time [min]	Build-up Rate [mm/min]	R^2
CMT	High	127.0	26.0	101.0	0.54	0.9973
CMT	Low	135.2	31.5	103.7	0.51	0.9993
MAG	High	147.7	28.6	119.1	0.48	0.9963
MAG	Low	144.8	35.8	109.0	0.46	0.9975

Table 4
Derived average build time rates, welding time rate, and the waiting time rate for the deposition of AM structures with different welding techniques and energy inputs, derived from Table 3 and Fig. 4.

Process	Energy Input	Build Time Rate [min/mm]	R^2	Welding Time Rate [min/mm]	R^2	Waiting Time Rate [min/mm]	R^2	Ratio
CMT	High	1.84	0.9973	0.37	1	1.47	0.9958	4.0
CMT	Low	1.97	0.9993	0.45	1	1.52	0.9988	3.4
MAG	High	2.17	0.9975	0.41	1	1.76	0.9962	4.3
MAG	Low	2.09	0.9963	0.51	1	1.58	0.9935	3.1

MAG process).

The corresponding representative values for the build time, welding time, waiting time and derived rates for each configuration are listed in Tables 3 and 4, respectively. The total build time of the parts was about 135.2 min and 127.0 min for the low and high energy input with CMT, respectively, and about 144.8 and 147.7 for the low and high energy input with MAG. The reduced average build-up rate of the MAG process required more layers, resulting in extended welding times compared to the CMT process. Although the welding time is extended, the waiting time is also due to the increased number of layers and increased heat input by similar material input as compared to those in the CMT process. Comparing the high to the low energy input for both processes, it can be seen that, although fewer layers are required, the waiting time per millimetre height increases in relative terms. While the waiting time rate to welding time rate is 3.1 and 3.4 for low energy input, it is 4.0 and 4.3 for high energy input, respectively. In addition, no distinct differences in the waiting time rate within the AM structure as a function of height can be seen, namely in the lower and upper layers ($R^2 > 0.99$). This can be assigned to the pre-heating condition of the substrate to 400 °C, which is in a similar temperature range as the interlayer temperature of the AM structures of 350–400 °C. Therefore, heat dissipation by conduction based on the temperature gradient within the solid volume may be comparable.

3.2. Chemical composition

Table 5 lists the actual as well as the nominal chemical composition of the filler wire, and Table 6 lists the chemical composition of the AM structures determined by atomic absorption spectroscopy. Considering the main alloying elements and the carbon content, no significant differences could be detected in the chemical composition between the processes and the different energy inputs for the AM structures. Even though a different shielding gas, i.e. active gas content, was used for MAG welding, this did not alter the results significantly. Therefore, it can be concluded that the final chemical composition and element loss of the AM components is independent of the process and process parameter range. Comparing the actual composition of the AM structures/filler wire to the nominal composition of the filler wire (Table 1), it can be seen that the amounts of the main alloying elements, chromium and molybdenum, are reduced. These deviations may be attributed to manufacturing tolerances, since welding consumables are usually subject to a tolerance with regard to their chemical composition, and the measured values fall within these tolerances. However, in the present study, the decrease in the amount of alloying elements is mainly restricted to the ferrite stabilizer, i.e. this leads to a significantly lower chromium equivalent Cr_{eq}.

Based on Table 6 and Equations (1) and (2), the chromium and nickel equivalents can be calculated for the AM structures consisting entirely of the filler wire material (nominal/actual chemical composition filler wire listed in Table 5). For CMT, Cr_{eq} 9.29% and Ni_{eq} 5.48% are obtained at low energy, and Cr_{eq} 9.42% and Ni_{eq} 5.62% are obtained at high energy, respectively. Regarding MAG, Cr_{eq} 9.33% and Ni_{eq} 5.46% are obtained at low energy, and Cr_{eq} 9.28% and Ni_{eq} 5.15% are obtained at high energy, respectively. The reduction in molybdenum and chromium in the AM structures compared to the nominal composition of the filler wire results in a lower chromium equivalent. Higher carbon content and the presence of nickel, which is not mentioned in the nominal chemical composition of the filler wire, were measured in the AM structures, resulting in a higher actual nickel equivalent of the AM structures compared to the values derived from the nominal composition of the filler wire (nominal filler wire: Cr_{eq} 10.40% and Ni_{eq} 3.30%).

3.3. Microstructural characterization

Representative microstructures are shown in Fig. 5. No significant macroscopic differences in microstructure between the investigated configurations. The microstructure consists of an α/α′-matrix, a finely distributed vermicular δ-ferrite network, and occasional larger polygonal δ-ferrite islands. According to the Schaeffler diagram (Fig. 1), the actual chemical composition of the filler wire and the reduction of ferrite-stabilizing elements would be sufficient for a martensitic microstructure. Nevertheless, the experimental results deviate marginally from this, and a minor fraction of δ-ferrite remains.

The representative character of the matrix was further observed by TEM on thin films and is shown in Fig. 6 for the CMT low-energy input sample. The matrix consists of predominantly very fine lamellae with a high dislocation density and a width of approx. 500–1000 nm. The orientation of the lamellae varies and is either uniformly parallel or differently oriented. Small amounts of laminar-like retained austenite were found between the laths. Twin-type martensite, in addition to a lamellar structure, was also observed, and SAED was used to index them. Dark-field images were taken considering the diffraction points $(020)_{austenite}$ (Fig. 6d) and $(110)_{martensite}$ (Fig. 6f).

In addition, the electron diffraction pattern of $M_{23}C_6$ was indexed (Fig. 6d). As can be seen in the TEM thin foils (Fig. 6a and b) and SEM images (Fig. 10a–d), spherical particles/cavities (indicated by arrows in Fig. 6a and b) are uniformly distributed throughout the cross-section. Randomly dispersed non-metallic inclusions (NMI) were formed during the AM process, and the NMI have an diameter of around 1 μm or less. The EDXS element distribution is shown in Fig. 7, and indicate that the NMIs are silicon- and manganese-based oxides (Fig. 7).

Fig. 8a–f shows the EBSD results for the matrix of the AM structures produced by applying the two different techniques and using a low-energy input. The inverse pole figure (IPF) maps in Fig. 8a,d shows the colonies of the α/α′ structure. The kernel average misorientation (KAM) maps in (Fig. 8b,e) and boundary maps (Fig. 8c,f) display the

Table 5
The actual chemical and nominal composition in wt.% of the filler wire X10CrMo6-3.

Filler Wire X10CrMo-3	C	Cr	Mo	Mn	Si	Ni	Fe	Cr_{eq}	Ni_{eq}
Actual	0.12	6.01	3.19	0.60	0.33	0.12	bal.	9.69	3.96
Nominal	0.10	6.50	3.30	0.60	0.40	–	bal.	10.40	3.30

Table 6
The actual chemical composition in wt.% of the CMT and MAG fabricated AM structures as measured by optical emission spectroscopy (OES).

Process	Energy Input	C	Cr	Mo	Mn	Si	Ni	Fe	Cr_{eq}	Ni_{eq}
CMT	Low	0.1685	5.880	2.970	0.490	0.295	0.175	bal.	9.29	5.48
CMT	High	0.1735	5.920	3.045	0.490	0.300	0.170	bal.	9.42	5.62
MAG	Low	0.1685	5.880	3.025	0.470	0.285	0.170	bal.	9.33	5.46
MAG	High	0.1580	5.865	2.975	0.485	0.290	0.170	bal.	9.28	5.15

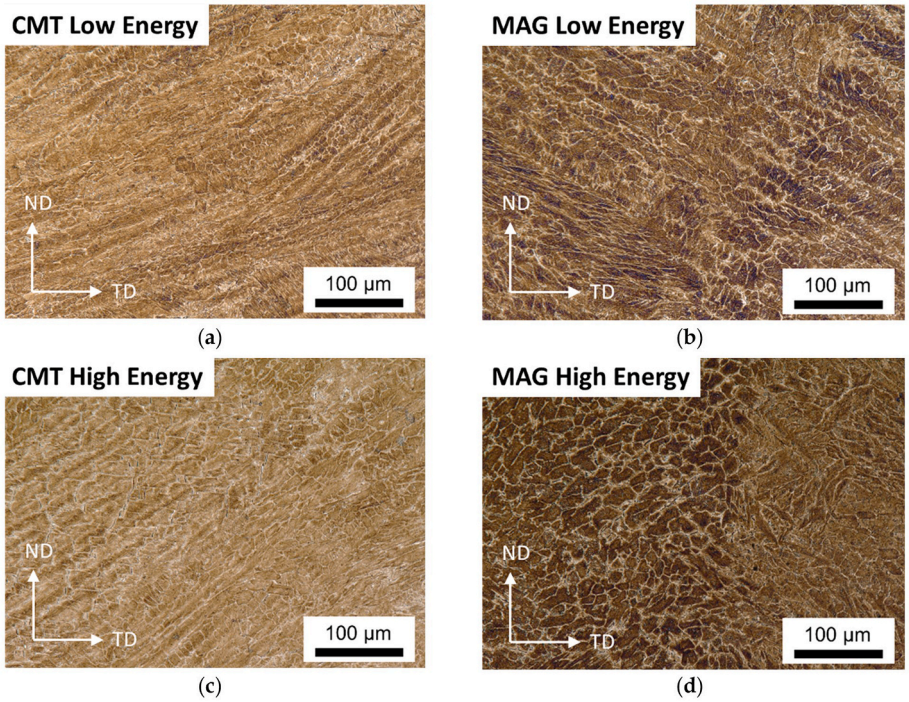

Fig. 5. Microstructures of AM structures made by using the arc welding technique CMT (a,c) and MAG (b,d) with low (a,b) and high (c,d) inputs; The micrographs were captured from specimens extracted from the center of the AM structures, i.e., from the central weld track at the mid-height of the structures.

intricate α/α′ structure with a high level of local misorientation. The maps in Fig. 8a–f reveal a comparable microstructure formed by the CMT and MAG processes with a low energy input. The microstructures of the AM cross-section of the AM structures produced by using the two different techniques and a high energy input are shown in Fig. 8g-l. As when using a low energy input, the α/α′ structure colonies compose the microstructure (Fig. 8g,j). The local misorientation (Fig. 8h,k) within the α/α′ matrix is higher than for the low energy conditions. The difference is more pronounced for the CMT (Fig. 8b compared to Fig. 8h).

Complementary to Figs. 8 and 9 quantifies the microstructural features of the measured conditions. Fig. 9a shows the geometrically necessary dislocation (GND) density distributions for the CMT and MAG AM samples with low and high energy input. Fig. 9b shows the misorientation angle distribution; The misorientation distributions show comparable similar values for misorientation angles smaller than 15° (subgrain boundaries) and for angles smaller than 5°. It indicates that the substructure, related to the fine α/α', is comparable for all depositions.

The difference in the GND density distribution between MAG AM samples with low and high energy inputs is minimal compared to the difference between CMT AM samples. The distribution of low and high angle grain boundaries, and consequently the substructure size, is related to the block and lath sizes of the α'. The thinner the α′ laths and the more intricated the block structure is, the finer and more intricated the substructure is. Considering one cooling cycle, the α′ block and lath sizes are related to the achieved cooling rates. The faster the cooling, the finer the block and lath sizes of the α'. Fig. 8 shows that The density of low-angle grain boundaries (LAGB) is markedly higher for the CMT with a high energy input (Fig. 8i) as compared to that with a low energy input (Fig. 8c). It shows that the cooling rates were smaller in the CMT with low energy input compared to the high energy input (Fig. 4b, Table 4). Fig. 8h,i shows a higher local misorientation values (higher KAM values) for CMT with a high energy input, which is also visible in the GND density distributions in Fig. 9a. Thus, the higher cooling rates achieved in the CMT with high energy input produced a α/α′ matrix with a finer, more intricate, with higher local misorientation and GND density values than the CMT with a low energy input.

The secondary phase δ-ferrite is embedded in the matrix in all samples for both predominantly vermicular and, to a lesser extent, polygonal forms (Fig. 10). The finely distributed vermicular δ-ferrite has a width of approximately 1 µm in all configurations. The EDXS element distribution shows the segregation of the ferrite-stabilizing refractory molybdenum, while the distribution of the ferrite-stabilizing chromium and austenite-stabilizing nickel remains comparatively constant (Fig. 11). In previous studies [23], similar behaviour was observed for molybdenum segregation. However, as the nickel content in the hot work tool steel increased, a more pronounced element partitioning was also observed for nickel and chromium, in contrast to what is observed in present study. The interface between the molybdenum-rich δ-ferrite with limited solubility of carbon and the carbon-enriched matrix is characterized by precipitates covering the grain boundaries. TEM observation with carbon replicates confirmed intense precipitation. TEM observations reveal the precipitation of precipitates with different morphology, size, and density. The precipitates could be generally

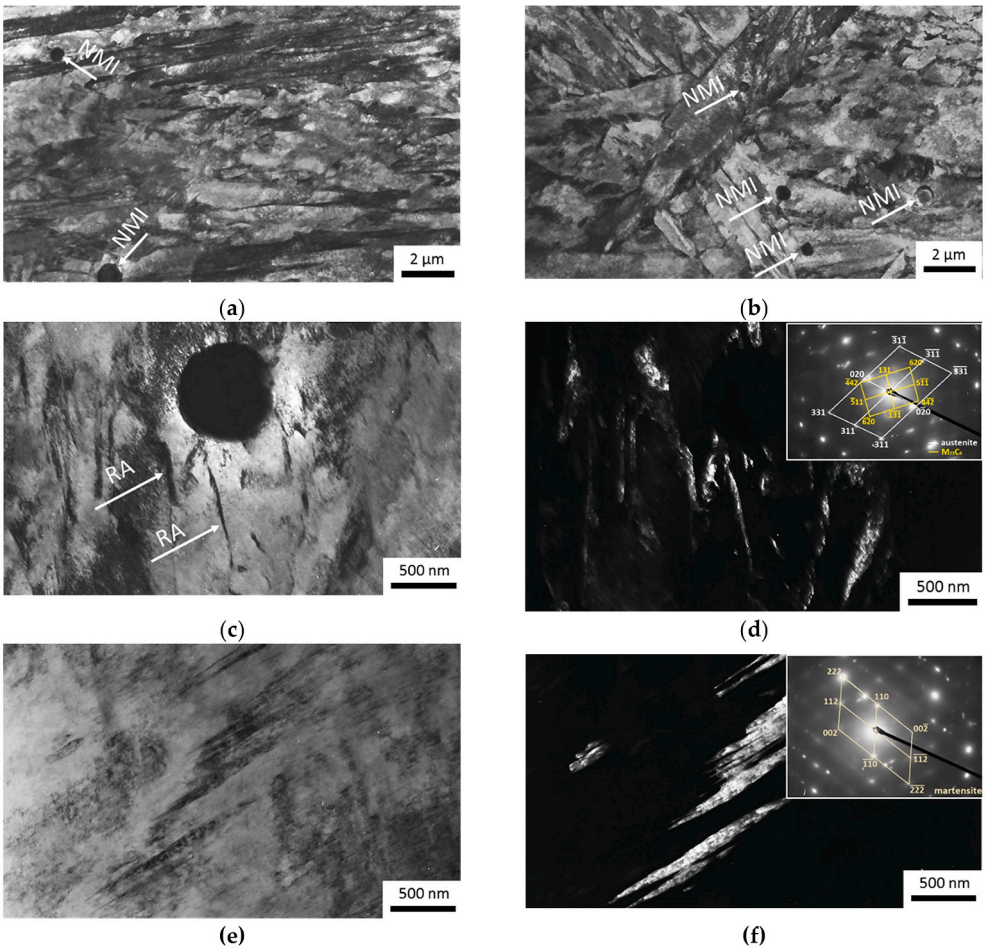

Fig. 6. Overview pictures of the matrix showing very fine laths with a high dislocation density in (a) uniform and (b) different orientations; non-metallic inclusions (NMI) are embedded in the matrix (marked by arrow). Detailed images of the additional matrix show (c) the presence of small fractions of retained austenite (RA) between the laths (marked by arrow) and (e) the presence of twin-type martensite indexed by selected area electron diffraction (SAED) on associated dark-field images (d,f).

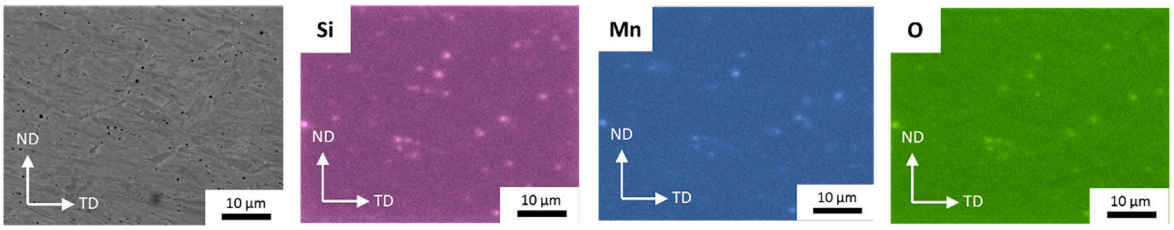

Fig. 7. Scanning electron micrography of a cross-section from CMT with low energy input and corresponding energy dispersive X-ray element distribution for silicon, manganese and oxygen, showing that the non-metallic inclusions are silicon- and manganese-based oxides. (For interpretation of the references to colour in this figure legend, the reader is referred to the Web version of this article.)

classified into two types: those forming 1) at the boundaries/inside the laths of the matrix and those forming 2) at the grain boundaries of the δ-ferrite.

Type 1 precipitates are small, needle-shaped particles observed inside the laths which are confined to zones with morphological features similar to that of lower bainite (Fig. 12b, Fig. 13a and b). The length of the single needles is about 200 nm or less, they are randomly oriented, and they can be clustered. High-resolution elemental mappings and spots scans identified them as iron-based and enriched in chromium and molybdenum main alloying elements as compared to the matrix (Fig. 14). The average composition of the main elements of the single and clustered needle-shaped particles is listed in Table 7. The weight percentage is approx. 79–81% for iron, 10–14% for molybdenum, and 8–9% for chromium, respectively. The second precipitate zone is confined to the interface between the δ-ferrite and matrix (Fig. 13c and d). The morphology of the precipitates varies along the grain boundaries of the δ-ferrite and can be classified as either blocky, needle-shaped, or irregularly shaped. The chemical composition of these precipitates also varies, with the smaller blocky particles being based on molybdenum-iron (Fig. 15, number 3). In contrast, the larger irregularly shaped and clustered (Fig. 15, number 2) and fine, needle-shaped particles (Fig. 15, marked by arrow) are based on molybdenum-chromium. The compositions measured in each case are listed in Table 8.

X-ray diffractograms of the cross-sections in the ND-TD plane

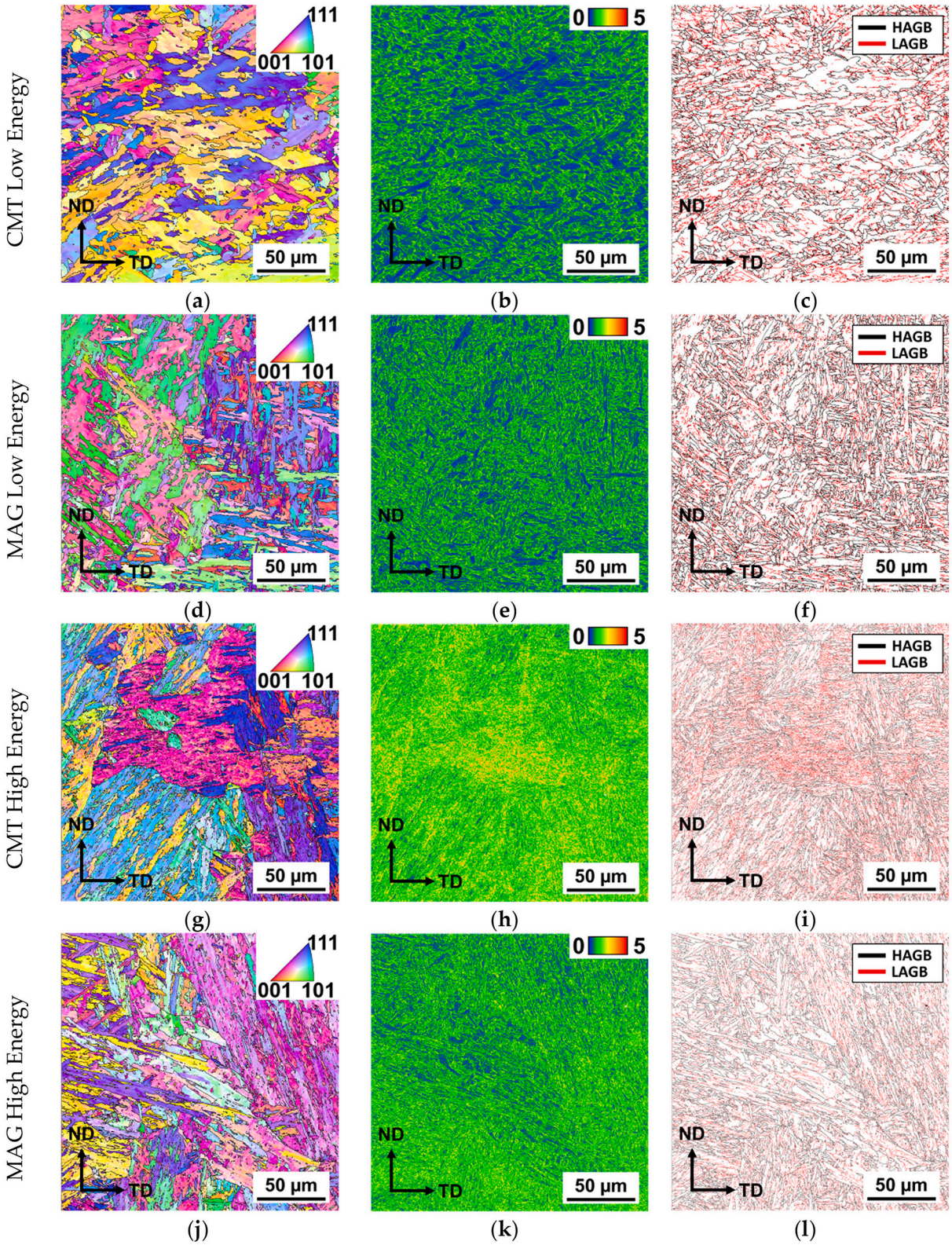

Fig. 8. Electron backscatter diffraction (EBSD) analysis of the AM samples fabricated with low energy CMT (a–c), low energy MAG (d–f), high energy CMT (g–i) and high energy MAG (j–l) arc techniques; (a,d,g,j) inverse pole figure (IPF) maps; (b,e,h,k) kernel average misorientation (KAM) maps; (c,f,I,l) boundary maps where black and red lines indicate high- and low-angle grain boundaries, respectively. Identical investigated position in the AM structures (centre), similar view field for all images a-l. (For interpretation of the references to colour in this figure legend, the reader is referred to the Web version of this article.)

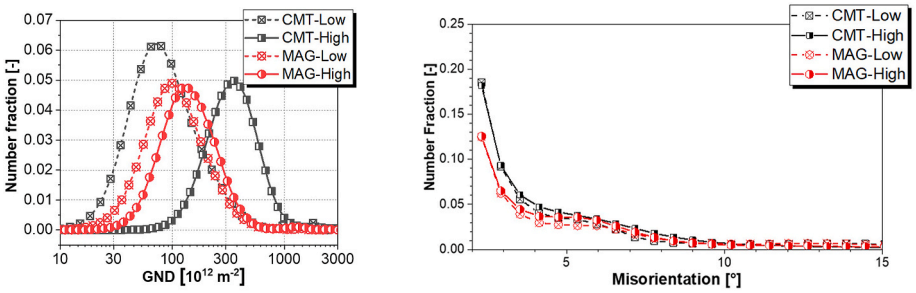

Fig. 9. Microstructure features of the matrix for the configurations CMT and MAG with low and high energy inputs: a) Geometrically necessary dislocations (GND) distribution; b) misorientation angle distribution.

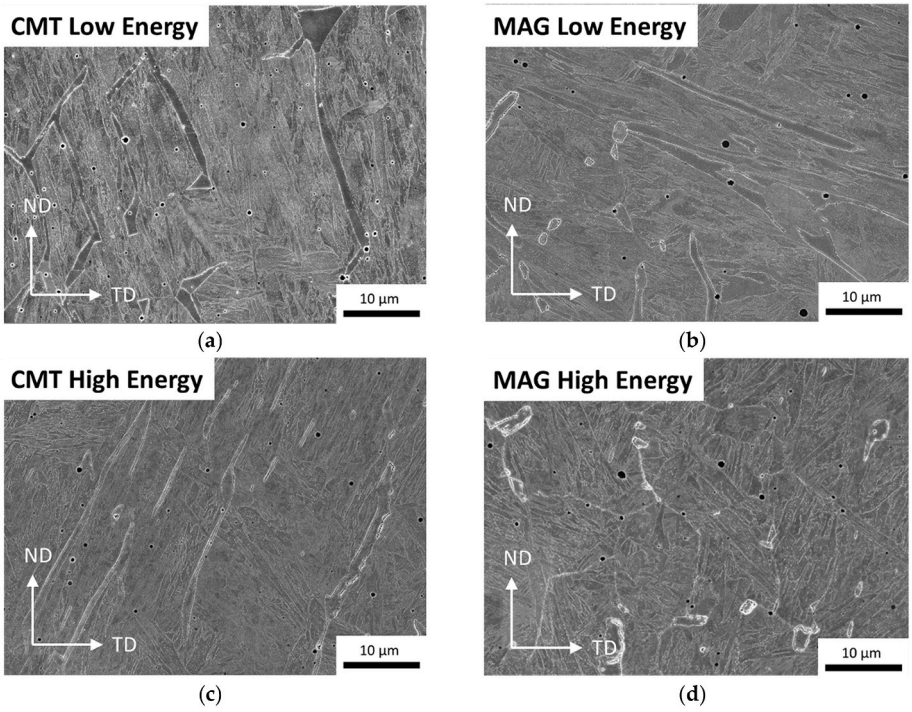

Fig. 10. Scanning electron micrographs of representative microstructures of AM structures, containing α/a' matrix and δ-ferrite, made with the arc welding technique CMT (a,c) and MAG (b,d) with low (a,b) and high (c,d) energy inputs.

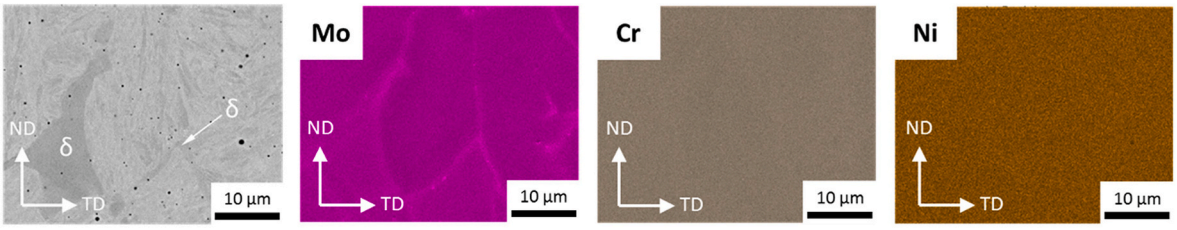

Fig. 11. Scanning electron micrograph and EDX element mapping for the ferrite-stabilizing elements molybdenum and chromium, as well as for the austenite-stabilizing element nickel. Segregation of the refractory molybdenum and enrichment in polygonal and vermicular δ-ferrite.

prepared by the low and high energy input for the CMT and MAG process are shown in Fig. 16. Out of all samples, only bcc α-iron is indicated, as diffraction peaks (110), (200), (211) and (220) were detected. These diffraction peaks can be assigned to the bcc/bct crystal structure, indicating that the fcc crystal structure is present only in a small fraction that cannot be detected with the XRD measurements. Therefore, the presence of retained austenite, as observed in a laminar form between the laths, is negligible in this work.

3.4. Mechanical characterization

3.4.1. Hardness measurements

The hardness maps of the ND-TD cross-sections and the average hardness values are shown in Fig. 17a and b as a function of the height of

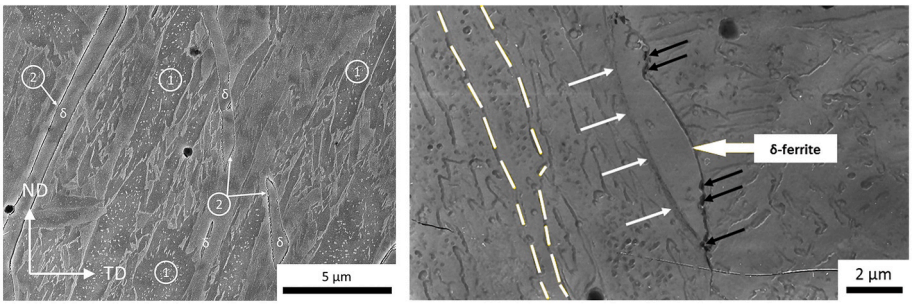

Fig. 12. (a) Scanning electron micrograph of the microstructure showing intense precipitation inside the laths of the matrix (1) and along the δ-ferrite grain boundaries (2); (b) transmission electron microscope on carbon replica, particles with different morphology were observed at the grain boundaries of the δ-ferrite; on the right-hand side, bigger particles of irregular shape (marked by black arrow) and high density of small needle particles were observed at the left side (marked by white arrow). A dashed line delaminates an area morphologically similar to the lower bainite, showing also precipitates.

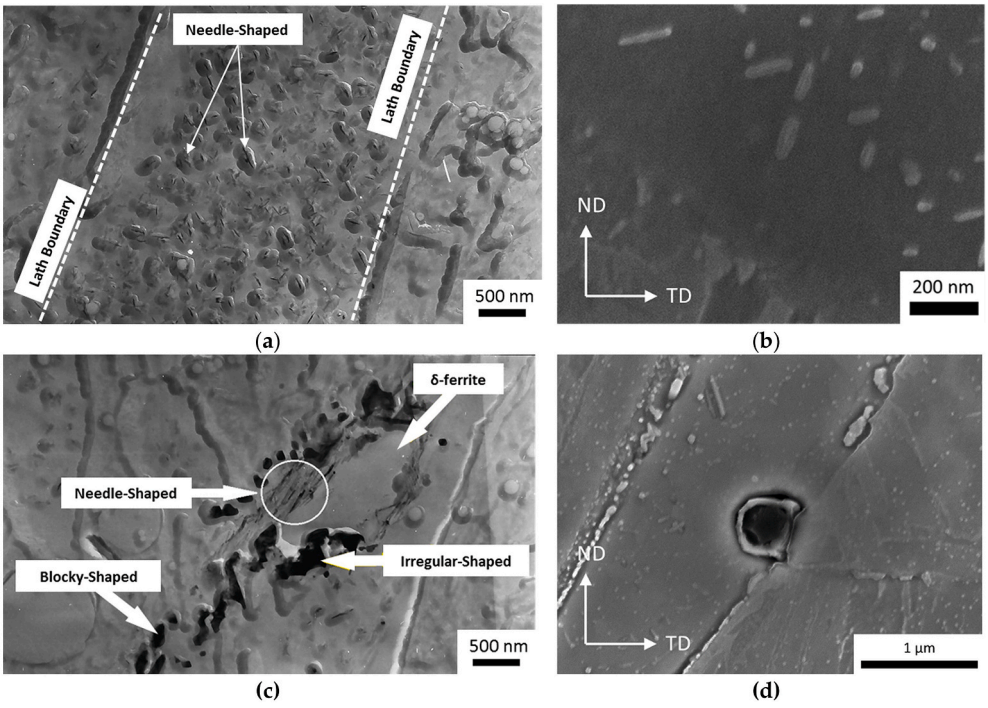

Fig. 13. (a) Transmission electron microscope (TEM) on carbon replica – detailed view of the area, which is morphologically similar to that of the lower bainite, high density of small needle particles was observed inside the lath and (b) related scanning electron micrograph (SEM) of the particles inside the lath (c) TEM on carbon replica - detailed view of different particles at the grain boundaries of δ-ferrite with varying morphology and (d) related SEM of the precipitates covering the grain boundaries.

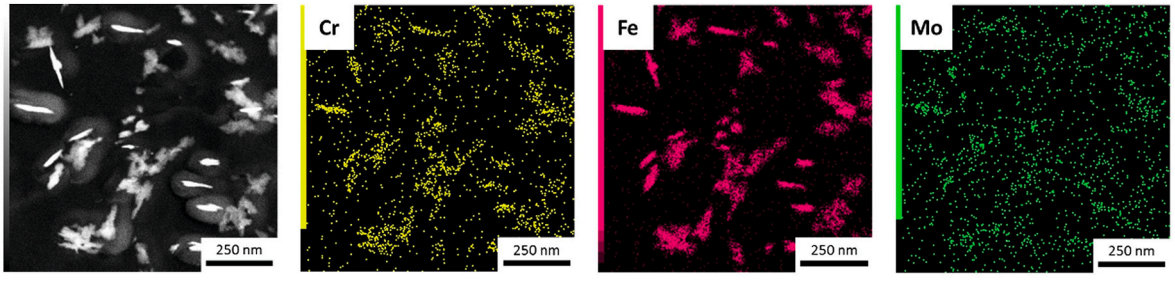

Fig. 14. High-angle annular dark-field (HAADF) image and EDX element mapping for main elements chromium, iron, and molybdenum of the precipitates located within the laths of the matrix.

Table 7
Average chemical composition in wt.% of the main elements chromium, iron, and molybdenum for the single and clustered needle-shaped iron-based particles located within the laths of the matrix shown in Fig. 14.

Morphology	Cr	Fe	Mo
Small Needle Particles	7.6	78.8	13.6
Cluster of Needle Particles	9.1	81.0	9.9

the AM structures. In general, each sample was found to have a macroscopically homogeneous degree of hardness in both height as well as width, with only some randomly scattered hardness changes predominately observed within the standard deviation range (Fig. 17a and b). The mean hardness values are 389 ± 48 HV1 and 392 ± 48 HV1 for the CMT process with low and high energy inputs and 382 ± 47 HV1 and 381 ± 82 HV1 for the MAG process with low and high energy inputs, respectively. The reference is the quenched and tempered substrate AISI H11 with a specified hardness of 400–440 HV. The mean hardness per layer remains nearly constant and does not deviate greatly from the average hardness of the whole cross-section (Fig. 17b). No visible tempering/softening effect was observed by subsequently layering weld beads on the preceding ones. The hardness in the upper layers, i.e. the last weld beads, does not vary significantly from the average hardness values of the whole section (Fig. 17b dashed lines) and is within the range.

3.4.2. Impact toughness

Charpy impact tests were performed on vertically (designated fracture plane WD-TD) and horizontally (designated fracture plane ND-TD) oriented V-notched specimens at room temperature. The absorbed impact energy as a function of the welding process, process parameters, and test direction is shown in Fig. 18. The absorbed impact energy values in the WD-TD plane (vertical) are 11.3 ± 1.2 J and 8.7 ± 2.3 J for CMT and 12.0 ± 3.0 J and 10.3 ± 2.1 J for MAG with low and high energy inputs, respectively. The absorbed impact energy values in the ND-TD plane (horizontal) are 10.7 ± 1.5 J and 7.7 ± 2.1 J for CMT and 10.7 ± 1.2 J and 9.7 ± 2.1 J for MAG with low and high energy inputs, respectively. The reference is the quality heat-treated base material AISI H11 with a measured absorbed impact energy of 14.2 ± 1.9 J. The fractured specimens did not show pronounced lateral expansion. No significant differences between the absorbed impact energy in WD-TD and ND-TD plane for the respective configurations were observed, but high energy specimens tended to have slightly lower impact energy.

3.4.3. Tensile properties

The tensile properties of the AM structures were determined vertically (load-direction: ND, designated fracture plane WD-TD) and horizontally (load-direction: WD, designated fracture plane ND-TD). The tensile strength as a function of the welding process, parameter configuration, and direction is shown in Fig. 19. The yield strength values are 1065 ± 55 and 1118 ± 63 MPa in the WD-TD plane (vertical) and 988 ± 21 and 1105 ± 77 MPa in the ND-TD plane (horizontal) for the CMT process with low and high energy inputs, respectively. The ultimate tensile strength values are 1383 ± 10 and 1306 ± 115 MPa in the WD-TD plane (vertical) and 1285 ± 99 and 1257 ± 137 MPa in the ND-TD plane (horizontal) for the low and high energy input CMT process. The yield strength values are 1083 ± 54 and 1125 ± 11 MPa in the WD-TD plane (vertical) and 1045 ± 72 and 1048 ± 111 MPa in the ND-TD plane (horizontal) for the MAG process with low and high energy inputs. The ultimate tensile strength values are 1384 ± 35 and 1333 ± 113 MPa in the WD-TD plane (vertical) and 1364 ± 29 and 1228 ± 251 MPa in the ND-TD plane (horizontal) for the low and high energy input MAG process. The heat-treated base material AISI H11 with a measured tensile strength of YS 1103 ± 14 MPa and ultimate tensile strength UTS 1316 ± 5 MPa was used as reference value. The multidirectional tensile strength of the AM material is at the level of the quality heat-treated base material for all configurations.

Representative stress-displacement curves for vertically and horizontally oriented tensile samples for each configuration are shown in Fig. 20. In all cases, the stress plateau is reached in order to derive the ultimate tensile strength. No significant differences in strain/displacement were observed between the configurations, and the strain/

Table 8
The average chemical composition in wt.% of the main elements chromium, iron, and molybdenum for the particles shown in Fig. 15; needle-shaped particles in the matrix are labelled as 1 and particles located at the grain boundary of δ-ferrite are labelled as 2 as well as 3.

Nr	Morphology	Cr	Fe	Mo
1	Small Needle Particles Inside the Laths	11.2	71.8	17.0
2	Bigger Particles of Irregular Shape	23.6	2.0	74.4
3	Smaller Particles of Blocky Shape	7.9	24.5	67.6

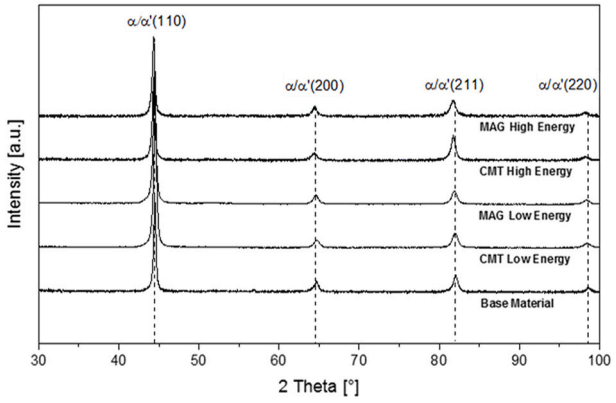

Fig. 16. X-ray diffraction patterns of the base material AISI H11 and AM structures made with CMT and MAG low and high energy input.

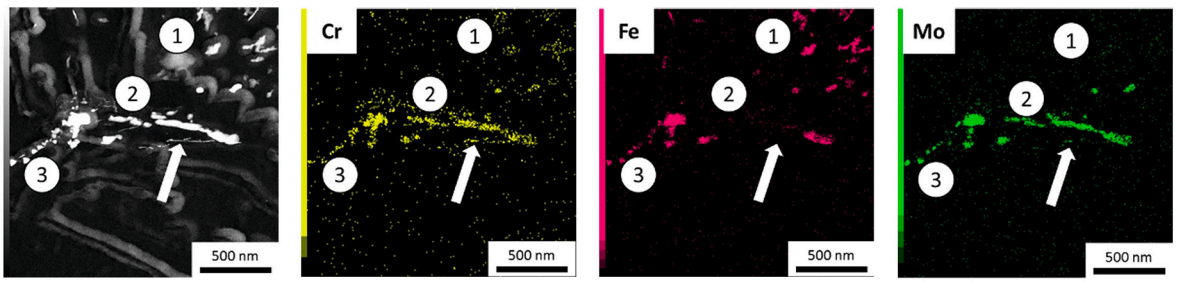

Fig. 15. High-angle annular dark-field (HAADF) image and EDX element mapping for main elements chromium, iron, and molybdenum of the precipitates located at the interface δ-ferrite and matrix (labelled as 2 for irregular-shaped and 3 for blocky-shaped, arrows indicate the needle-shaped precipitates) and in the laths of the matrix (labelled as 1 for needle-shaped precipitates).

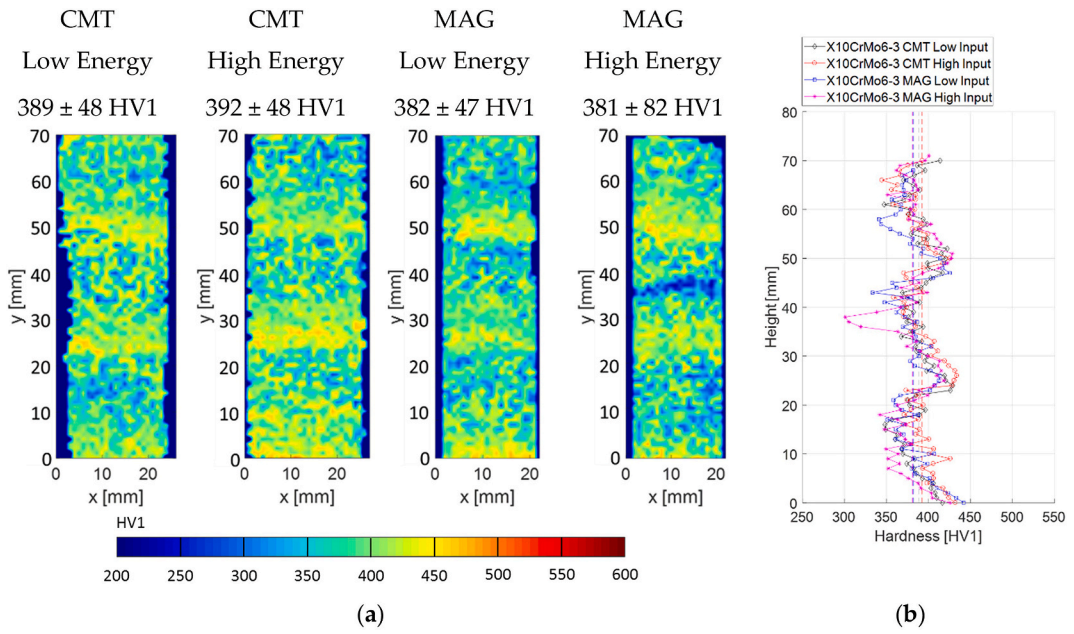

Fig. 17. (a) Hardness distribution in the ND-TD plane of the AM bulk material for different welding processes and energy inputs; (b) corresponding mean hardness levels depending on height (markings) and mean hardness of the AM material for the respective configuration (dashed line).

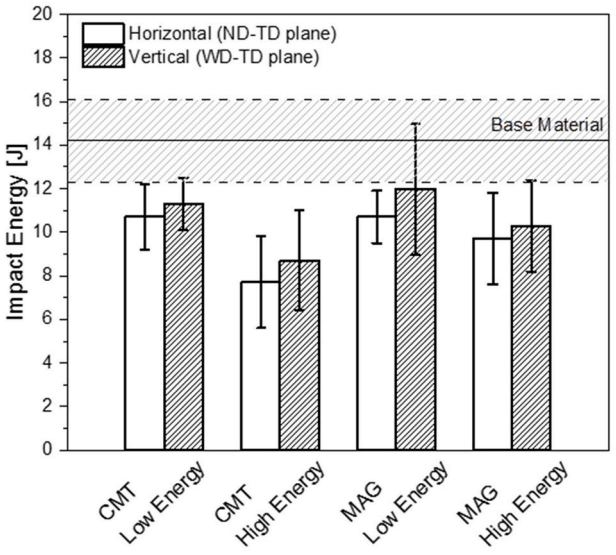

Fig. 18. Absorbed impact energy at room temperature in the vertical (fracture plane WD-TD) and horizontal (fracture plane ND-TD) orientations of AM parts made with CMT and MAG process with different energy inputs; solid and dashed lines represent the measured average impact toughness and its standard deviation.

displacement is comparably low. A total displacement of less than 3 mm until fracture was achieved, while a plastic deformation of less than 2 mm was observed for the total specimen length of 60 mm. All fractured specimens show no signs of significant necking.

4. Discussion

4.1. Material deposition

To make representative comparisons between the processes, the parameters for both processes were chosen to achieve similar material deposition (wire feed rate), i.e. once 5.4 m/min at low energy input and once 7.2 m/min at high energy input. Due to the intrinsic properties of the CMT process, the periodic retraction of the wire results in mechanical drop support, which leads to an calculated energy input reduction of about 20% for the same material input as compared to that in the MAG process. In addition to the CMT process's lower energy input, the weld bead geometry changes significantly as compared to the weld beads deposited with the MAG process. While the beads deposited with MAG tend to be wider and flat, the beads deposited with CMT are narrower and higher.

Oliveira et al. [68] compared standard CMT and GMAW methods for the WAAM process on ER70S-6 mild steel using the same measured/actual heat input per unit length; a 28% higher material deposition rate for CMT could be achieved (8.17 m/min CMT and 6.39 m/min GMAW). In addition, good agreement was found between the nominal average values of the process parameters and the actual measured values, allowing estimation of the actual heat input by deriving it from the nominal ones. Similar to the present study, more pronounced weld beads are observed when applied by the standard CMT method than by the GMAW. Oliveira et al. [68] attribute this to the low heat input and rapid solidification of the CMT process over GMAW. Galeazzi et al. [69] compared variants of the CMT process with the conventional GMAW process for martensitic WAAM AISI 420 stainless steel; the focus was particularly on very low deposition rates, i.e., 1.7 m/to build thin-walled structures. In the CMT process, the instantaneous power at the time of arc reopening is reduced to 75% compared to the conventional GMAW process, due to the combination of wire movement and current modulation control. The CMT process and the conventional GMAW process produced good and significantly similar results, with no significant difference in macroscopic morphology. However, CMT provided better arc stability, resulting in better control of final dimensions, metal transfer, and thus higher material and process efficiency; this is consistent with the present study. Prasanna Nagasai et al. [70] investigated the WAAM process for austenitic 308L stainless steel to produce cylindrical components using again the standard CMT and conventional GMAW processes. At a nominal wire feed rate of 5 m/min, the GMAW process required 27% more heat input per unit length (0.391 kJ/mm) than the CMT process (0.308 kJ/mm). In addition, fewer layers and faster build-up were possible with CMT, as the average layer height was 16% higher than with GMAW, which is in a similar range to the present

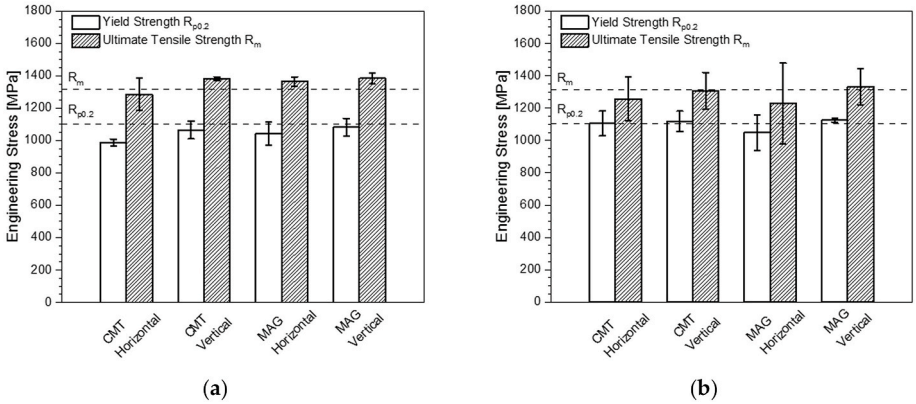

Fig. 19. Tensile strengths at room temperature for vertically (designated fracture plane WD-TD) and horizontally (designated fracture plane ND-TD) oriented tensile specimens of AM parts fabricated with CMT and MAG process with (a) low energy input and (b) high energy input; dashed lines represent the average tensile strengths of the quality heat-treated base material AISI H11.

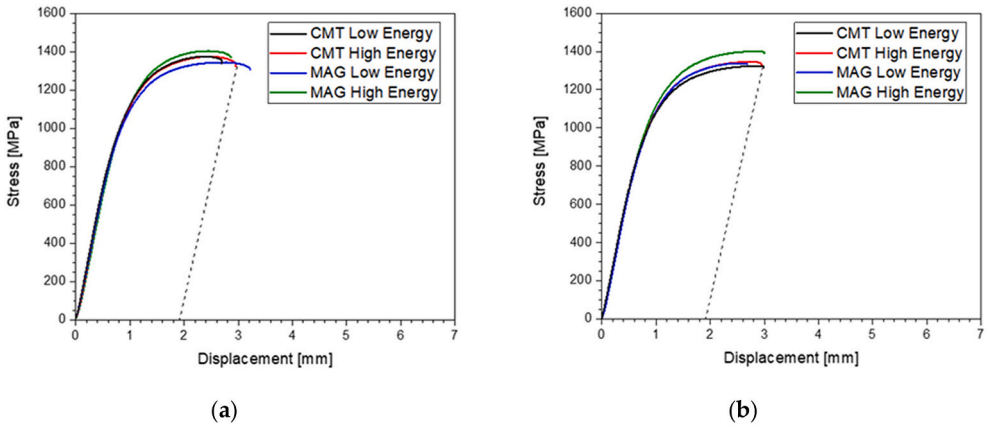

Fig. 20. Representative stress-displacement curves at room temperature for (a) vertically (designated fracture plane WD-TD) and (b) horizontally (designated fracture plane ND-TD) oriented tensile specimens of AM parts fabricated with CMT and MAG process with low energy input and high energy input; no clear differences in displacement are seen between configurations.

study. Prado-Cerqueira et al. [71] studied variants of CMT with conventional GMAW for ER70S-6; at a constant moderate wire feed rate of 2.5 m/min, lower heat input was found for CMT compared to GMAW, associated with a 13% higher layer height for CMT (1.02 mm CMT, 0.90 mm GMAW). The differences in heat input per unit length for the same material input in CMT and pulsed MIG processes is assigned to the different metal transfer mode [72]. Metal transfer by dipping, i.e., short-circuiting, lowers the penetration depth and heat input in CMT over pulsed GMAW, where metal deposition is usually by globular and spray transfer depending on the applied current or in pulsed form [72]. In the case of CMT, repeated cycles of switching the arc on and off, assisted by electronically controlled forward and backward movement of the feed wire, ultimately reduce arc energy and heat input, thereby reducing dilution and overall penetration depth. In pulsed GMAW technology, the wire is not retracted and the arc remains on all the time, although the current pulsing reduces the overall arc energy [72].

Consequently, CMT promotes a faster build-up process and higher structures. As a result, fewer layers were required to achieve the desired height and resolve the desired geometry. The overall energy input could be reduced in present study once the CMT process was applied. This corresponds to a reduction in the number of layers by about 10% in the CMT process as compared to the MAG process. The material transfer that takes place in the CMT process at a lower energy level is responsible for the lower welding temperature, i.e. waiting time, and less dilution with the substrate/preceding layers [47,73]. Due to its low heat input and dilution, CMT seems more suitable for AM than standard GMAW processes [47]. The lower heat input and dilution ensure continuous deposition and prevent the overheating or excessive remelting of previously deposited material [47]. By maintaining the defined interpass temperatures and build-up sequence, the CMT process achieves the fastest build-up rates (>10% faster than those in the MAG process).

4.2. Microstructure and chemical composition

No significant deviations were measured between the actual chemical compositions of the AM structures produced with different processes and parameters. Only some minor and negligible changes in individual elements were detected. These findings indicate that the welding techniques and the chosen material/energy input do not contribute significantly to the element loss, e.g. evaporation during AM of hot work tool steel grades. The scatter observed between nominal and actual chemical composition is more significant. The actual chemical composition of the AM structures deviates significantly from the nominal chemical

Table 9
Transformation temperatures for the X10CrMo6-3 filler wire/AM structures for nominal and actual chemical composition, calculated by using thermodynamic equilibrium calculations.

	A_1 [°C]	A_3[°C]	A_4 [°C]
Nominal Chemical Composition	839	984	1178
Actual Chemical Composition	823	907	1275

composition of the filler wire, and especially for the main alloying elements, ferrite-stabilizer Cr and Mo. In addition, an increased carbon content was measured after AM, which may be attributed to the active shielding gas containing CO_2. The nickel content was also increased, which benefits the formability/drawability of the filler wire; however, nickel is not listed in the nominal composition according to the datasheet [74] but measured in the actual composition of the filler wire. The 1) reduction in the fraction of main ferrite-stabilizing elements Cr and Mo, 2) increased carbon content, and 3) austenite-stabilizing element Ni lowers the Cr_{eq}/Ni_{eq} ratio. Thermodynamic equilibrium calculations performed with the nominal and actual chemical compositions show that the change in composition primarily enlarges the austenite region, lowers the equilibrium temperatures of A_1 and A_3, and increases A_4, Table 9. Fig. 21 *shows* the equilibrium phase fractions as a function of temperature for the nominal and actual chemical compositions. The equilibrium calculations show that the change between the nominal and actual chemical compositions has little effect on the phase fraction and solubility of precipitates $M_{23}C_6$ and MX. The calculations for these values remain fairly similar (Fig. 21a and b). A maximum equilibrium phase fraction of 3.7 mol.% $M_{23}C_6$ and 0.08 mol.% MX was predicted for the nominal composition by the simulation. The change in chemical composition primarily affects the $\alpha \rightarrow \gamma \rightarrow \delta$ transformation and vice versa. The added nickel and increased carbon content act as an austenite stabilizer in the chemical composition. In contrast, the Cr and Mo content (ferrite stabilizer) is reduced as compared to the nominal composition. This content increases the austenite range and alters the critical equilibrium temperatures A_1, A_3 and A_4, as shown in Fig. 21*c*.

The microstructure of comparable carbon-bearing hot work tool steels produced by wire- and powder-based AM processes depends on the applied process, process parameters, welding sequence, and interpass strategy. Ali et al. [38], Ge et al. [75], and Wang et al. [39] investigated WAAM on H11 and H13 tool steels, respectively. Ali et al. [38] described the influence of the selected interpass temperature on the properties of H11 a.m. components. If the interpass temperature is kept below Ms, fresh martensite and some retained austenite will form in the deposited layer as Mf is below room temperature. Subsequent layers heat treat the previous ones; this means that, when the austenitizing temperature is exceeded, martensite is converted back to austenite, and areas that do not reach the austenitizing temperature are tempered. The amount of retained austenite is thus reduced. Consequently, for carbon-bearing hot work tool steels, interpass temperatures below Ms lead to an undesirable graded microstructure and inhomogeneous properties unlike interpass temperatures above Ms, which produce homogeneous properties [38].

AM components are subjected to multiple thermal cycles during layer-by-layer metal deposition, affecting the local and global microstructure, and associated mechanical properties. Temperature control and thermal management are essential to achieve the desired material properties [72]. In WAAM, subsequent layer deposition is often started after a fixed idle time (e.g., Refs. [76,77]) has elapsed. However, depending on the size and shape of the AM component, a constant idle time may not be sufficient to control the temperature. Montevecchi et al. [77] consider that the main challenge in applying the idle time technique is to choose variable idle times depending on the layer/position to

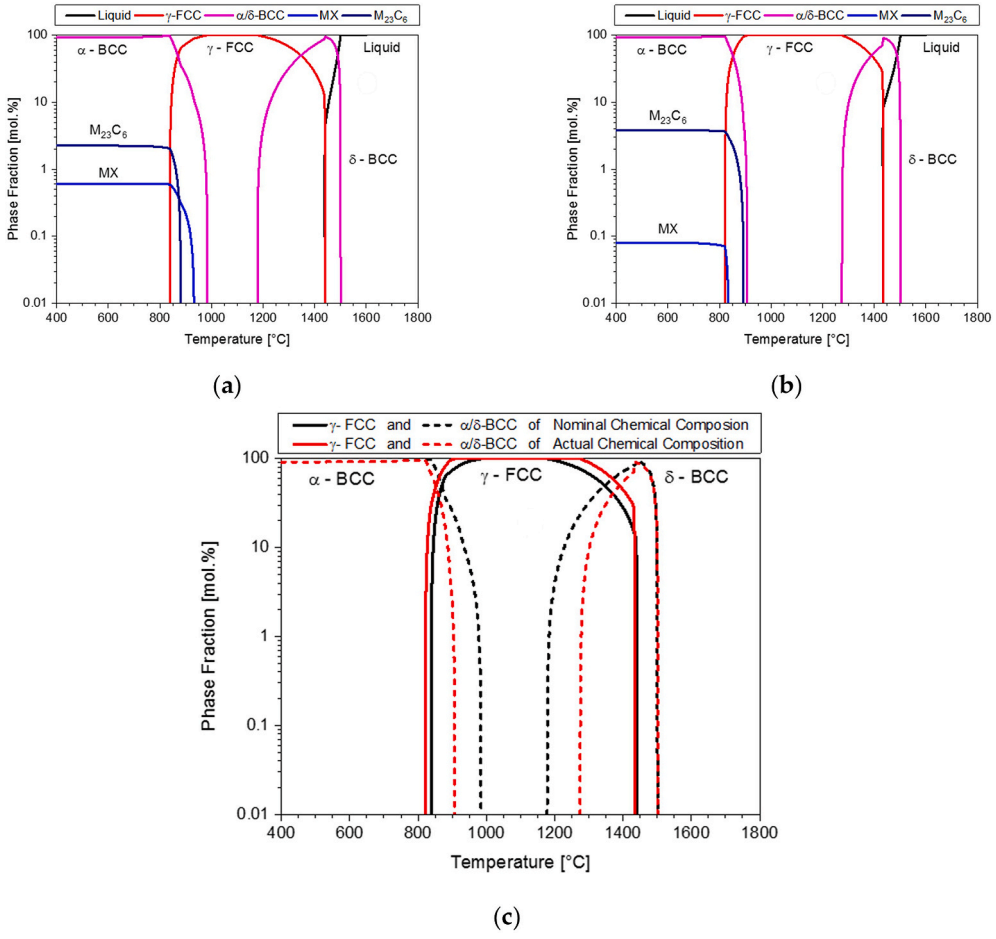

Fig. 21. Thermodynamic equilibrium simulations for the (a) nominal chemical composition of the filler wire and (b) actual chemical composition of the X10CrMo6-3 AM structures; (c) α-, δ-ferrite, and austenite phase fraction as a function of temperature for the nominal chemical composition (black) and actual chemical composition (red). (For interpretation of the references to colour in this figure legend, the reader is referred to the Web version of this article.)

ensure a constant interpass temperature, since the cooling rate of the workpiece changes throughout the process. Therefore, in the present study, the interpass temperature was directly monitored and the subsequent layer was deposited as soon as the required interpass temperature (above Ms) was reached. The results shown in the present work agree with those of Ali et al. [38]. For example, using an interpass temperature above Ms resulted in the creation of a comparable homogeneous microstructure and hardness distribution for the fabricated AM parts in the present study. Unlike to Ali et al. [38], no diffraction peaks for fcc by XRD were measured in the present work (although observed by TEM), indicating that the presence of retained austenite is negligible. As compared to the other carbon-bearing hot work tool steels H11/H13 (nominally 0.38 wt% and 0.40 wt%), the lower carbon content of the tool steel used in the present study, X10CrMo6-3 (nominally 0.10 wt%, actually 0.15–0.17 wt%), can explain the absence of the larger amount of retained austenite observed in this investigation. In carbon-bearing hot work tool steels (AISI H11/H13), the microstructure consists mainly of martensite and intercellular/interdendritic retained austenite (RA). The cellular structure is the result of constitutional undercooling accompanied by microsegregation leading to the concentration of alloying elements in the interdendritic regions [78]. Wu et al. [79] found that nickel, chromium, and molybdenum have effect on retained austenite, and Bajaj et al. [80] reviewed that in particular the enrichment of carbon stabilizes the austenite at room temperature in hot work tool steels. The retained austenite content increases linearly with decreasing Ms temperature, while high Ms temperatures lead to low final austenite contents [79]. Stabilization of RA at room temperature in the microstructure can be assumed if the final martensite temperature (Mf) of the alloy is below room temperature [81]. Fonseca et al. [82] performed atom probe tomography (APT) on L-PBF on H13 to locally resolve the chemical composition. Regions with C concentrations above 4 at.% are most likely parts of RA (about 3 vol%), while those with lower C concentrations are associated with fresh martensite. Interfaces exhibit local peaks of C, Cr, V, Mo, and Mn. These interfaces are assumed to be martensite/RA interfaces. The microsegregated microstructure at the cell walls exhibits a complex composition containing both austenite-stabilizing (C) and ferrite-stabilizing elements (Cr, Mo). The distribution of the elements, especially C, on RA locally lowers the Ms temperature and prevents the formation of a fully martensitic microstructure in the as-built condition [82]. In the present study, a low-carbon hot work tool steel alloy was used, which offers advantages such as a softer martensite, resulting in lower susceptibility to cracking and residual stresses, and allowing printing more complex geometries ([6,83]). Deirmina et al. [83] investigated such low-carbon hot work tool steels by comparing a conventional H13 grade (approx. 0.4 wt% C) with a carbon-lean H13 grade (0.25–0.30 wt%) in L-PBF. Both, conventional H13 and the modified composition, were characterized by a cellular dendritic solidification microstructure comprising an ultrafine martensitic matrix and microsegregation of alloying elements at the cellular/dendritic boundaries. The microsegregation resulted in stabilization of RA, however the RA content in the modified H13 alloy (2 vol%) was significantly lower than that of the conventional H13 (11 vol%), most likely due to the lower carbon content. The reduction of about 0.1 wt% C almost suppressed the formation of RA, retaining only a small amount of 2 vol% RA. In the present work and used filler wire alloy, not only the carbon content is lower compared to Deirmina et al. [83] but also the content of the ferrite stabilizing elements Mo and Cr is significantly increased.

Regarding the chemical composition, the filler wire grade used shows similarities with high-temperature creep resistant Cr-steels such as P91 (approx. 9 wt% Cr, 1 wt% Mo and a low carbon content of 0.1 wt %) and the stainless steel PH 13-8Mo (approx. 13 wt% Cr, 2 wt% Mo and 0.05 wt% carbon). Li et al. [84] observed an ultrafine martensitic matrix with fractions of δ-ferrite in WAAM of P91, and Ghaffari et al. [85] observed vermicular and lath δ-ferrite residues in a martensitic matrix in WAAM of PH13–8Mo. Moreover, in WAAM of AISI 420 (high chromium content of about 12–14 wt% and a carbon content of 0.15–0.40 wt%), Salahi et al. [86] and Lunde et al. [81] report a similar microstructure as before, namely δ-ferrite embedded in a martensitic matrix. The vermicular δ-ferrite phase formed along the prior austenite grain where higher concentrations of element Cr (a ferrite stabilizing element) and lower concentrations of iron are present. When the content of ferrite-stabilizing elements in the chemical composition of martensitic stainless steel predominates over austenite-stabilizing elements (as in the case of ER420 and the low-carbon hot work tool steel used in this study), it is possible that the high-temperature δ-ferrite phase is retained in the martensitic matrix at room temperature.

Considering the actual composition and the deviation of the Cr_{eq} and Ni_{eq} from the nominal chemical composition, it can be assumed that all AM structures are within the fully martensitic range close to the martensite + ferrite regime, i.e. without the presence of residual δ-ferrite, according to the Schaeffler diagram (Fig. 22). However, the AM structures' micrographs show a predominately fine vermicular δ-ferrite network embedded in an α/α′ matrix. No apparent difference in the morphology and proportion of δ-ferrite could be detected due to differences in the process or energy input. In AM processes, the material is generally rapidly molten, solidified, and quenched at extremely high rates, resulting in elemental micro-segregations. While the high solidification and cooling rates in the L-PBF process generally suppress δ-ferrite formation and cause the solidification of the austenite phase in hot work tool steels [87], the presence of δ-ferrite has been observed in H13 a.m. parts produced with the wire-based WAAM process [75]. In particular, in the overlap zone, i.e. the remelted zone of the adjacent weld traces, the microstructure is composed of a dual-phase consisting of 1) a blocky-like soft δ-ferrite, which has a large distribution in size, and 2) refined martensite was observed [75]. In the present study, soft δ-ferrite was also observed, which was homogeneously and finely distributed over the entire cross-section instead of being confined to specific zones (e.g. remelted areas). The selected hot work tool steel has an increased chromium and molybdenum content as compared to that of the H13 grade studied by Ge et al. [75], which promotes the segregation of certain elements and the stabilization of undesirable δ-ferrite [23,88].

Visible imperfections (e.g., cracks) were not detected in any of the AM cross sections examined, but randomly scattered non-metallic inclusions (NMIs), typically silicon- and manganese-based oxides, were seen. When active gas is used as a shielding gas, the alloying elements silicon and manganese have an affinity to react with oxygen, acting as getters and forming harmful silicon and manganese oxides [89–94]. As a result, non-metallic inclusions and oxides form especially to a large extent in AM-manufactured components; these then have a detrimental

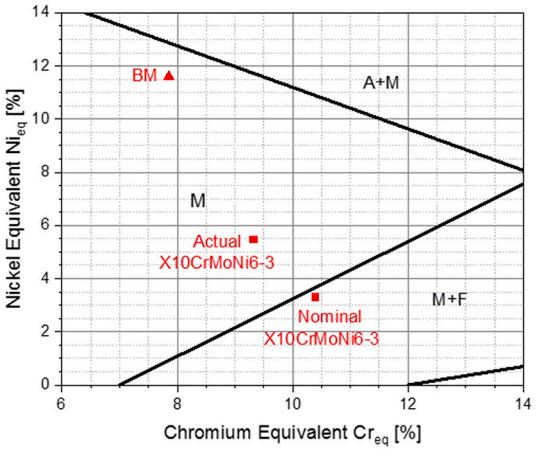

Fig. 22. Detailed view of the Schaeffler diagram and relevant materials are marked; differences between the nominal filler wire composition and the actual chemical composition are depicted; F.: ferrite, A.: austenite, M.: martensite, BM.: base metal.

effect on the mechanical properties, e.g. toughness and fatigue, of these components [95].

4.3. Mechanical properties

Similarities in the microstructures of the AM structures fabricated with the investigated processes and energy inputs are also evident when examing their mechanical properties. All AM structures had a reasonably homogeneous hardness distribution with an average Vickers hardness of about 380–390 HV1. The present results agree with those of Ali et al. [38]. Keeping the interpass temperatures above the martensite start temperature (Ms) in processing hot work tool steels forms microstructures with homogeneous hardness profiles along the building height. This finding contrasts with those of Plangger et al. [46] and Stockinger et al. [22], who reported that continuous heating-cooling cycles with temperatures below Ms in martensitic steel led to permanent tempering by the subsequent weld beads. As a result, an increase in the hardness of the surface layers and an inhomogeneous hardness distribution could be observed as soon as the interpass temperature dropped below Ms. According to the manufacturing guidelines [60], a hardness of approx. 38–42 HRC in the untreated state can be expected for the filler wire, corresponding to the measured HV values converted into HRC (380 HV ~ 39 HRC). As comparison with similar 3D-printed hot work tool steels remains challenging due to the limited amount of available literature. Therefore, the hot work tool steel grade H11 (substrate) and H13 serve as a reference for the present investigation. The hardness of the wrought material H11 depends on the heat treatment applied (e.g. austenitization, tempering temperature duration) and representative hardness values are 50–56 HRC (513 HV–616 HV) in the hardened condition and ~54 HRC (578 HV) after annealing twice at 500 °C. When H11 is processed by powder- and wire-based methods, the hardness in the "as-built" condition varies. For example, reported hardness values range from 500 to 730 HV, and representative values are listed in Table 10. In general, the hardness level of the wrought and powder-based 3D-printed substrate H11 is higher than that of the wire-based printed X10CrMo6-3, partly because the chemical compositions differ. In addition, the proportion of soft δ-ferrite contributes to the hardness; the higher the δ-ferrite proportion, the lower the average hardness [23].

In hot work tool steels, Cr, Mo, and V are added to increase hardenability and promote carbide formation, depending on the chemical composition and heat treatment applied. The carbon content of the H11 substrate differs and is significantly higher (about 0.38 wt%) than that of the X10CrMo6-3 filler wire, and V is also added to promote the formation of MC. The metal matrix's vanadium-rich MC and chromium-rich M7C carbides contribute to and increase wear resistance and hardness [96–98]. However, the AM of hot work steels remains challenging due to their high carbon content, which increases their susceptibility to cracking during deposition, which has been attributed to residual stresses. Regarding L-PBF, this susceptibility to cracking can be reduced by preheating the build platform [18], but cracking can still occur. Casati et al. [6] found that a low-carbon composition of hot work tool steel may be useful when the 3D printing complex parts by using L-PBF. These parts are then expected to have higher toughness and damage tolerance to residual stresses and processing defects. A lean version of H11 tool steel with a 30% carbon reduction (i.e. 0.24 wt%) resulted in a hardness level of 427 HV1 [6], which is comparable to the present results and the hardness level of 380 HV1 (89% of [6]) for AM structures with an actual carbon concentration of about 0.15–0.17 wt%.

The measured absorbed impact energy of the AM parts produced by WAAM is significantly higher than that of the samples produced by powder-based L-PBF processes from other carbon-bearing hot work tool steels (Table 11). The reasons for the comparatively low absorbed impact energy of L-PBF printed AM parts are manifold: 1) the residual stress level differs due to the rapid cooling rates influenced by the preheating conditions, 2) imperfections are introduced, causing, e.g. a lack of integrity due to partially melted particles or (cold) cracks, and 3) different proportions of retained austenite can occur due to complex thermal cycling and rapid cooling rates [102–105]. With regard to certain aspects, the applied WAAM processes differ significantly from the powder-based L-PBF process, leading to comparably lower cooling rates and complete integrity [75] due to the intrinsic process characteristics and preheating level.

The tensile strengths slightly, but not significantly, increased when specimens were loaded in the perpendicular direction (vertical) as compared to specimens loaded in the direction parallel (horizontal) to the welding direction. The changes in tensile strengths shown in this work are still within the standard deviation ranges, indicating a significantly isotropic tensile strength. This may be attributed to the interpass strategy as well as the homogeneous, finely distributed δ-ferrite in the AM structures. In contrast, Lyu et al. [106] and Ge et al. [107] observed anisotropic tensile properties for martensitic stainless steel 2Cr13, and Wang et al. [39] and Ge et al. [75] observed these for the hot work tool steel H13 fabricated with WAAM. However, the anisotropic tensile

Table 10
Representative hardness levels according to literature for powder and wire-based 3d printed AISI H11 and H13 hot work tool steel grades.

Process	Feed Stock	Material	Interpass Strategy	Condition	Remark	Hardness	Ref.
L-PBF	Powder	H11	~380 °C	As-Built	–	642 ± 9 HV1	[18]
				Hardened	1100 °C/15min	737 ± 16 HV1	
				Annealed	1100 °C/15min + 2 × 550 °C/2h	585 ± 9 HV1	
L-PBF	Powder	H11	–	As-Built	–	~506 HV1	[6]
				Annealed	1010 °C/10min + 500 °C/2h	~548 HV1	
L-PBF	Powder	Lean H11	–	As-Built	–	~427 HV1	[6]
				Tempered	550 °C/2h	~486 HV1	
L-PBF	Powder	H13	100 °C	As-Built	–	620–670 HV 5	[99]
LMD	Powder	H11	–	As-Built	–	~730 HV0.5	[14]
				Tempered	3 × 570 °C/2h	~690 HV0.5	
				Annealed	1080 °C + 3 × 570 °C/2h	~600 HV0.5	
LMD	Wire	H11	–	As-Built	Single/Multitrack	~50/60 HRC	[100]
LMD	Wire	H11	–	As-Built	Single Layer	~700 HV0.2	[101]
CMT	Wire	H11	100 °C	As-Built	Zone A	500–600 HV1	[38]
					Zone B	~700 HV1	
			300 °C		–	~690 HV1	
			600 °C		–	~700 HV1	
CMT	Wire	H13	Interpass 60s	As-Built	Martensite Zone	475 HV	[75]
			Interlayer 300s		Martensite + Ferrite Zone	360 HV	
MIG	Wire	H13	150 °C	As-Built	–	300–360 HV	[39]

The absorbed impact energy in the ND-TD and WD-TD planes of AM specimens fabricated with low energy input is within the range of 10–12 J, which corresponds to 70–85% of the heat-treated H11 substrate and 64–76% of the heat-treated H13 substrate (15.7 J [102]), respectively.

properties can be attributed to a graded microstructure and hardness profile due to continuous deposition and in-situ micro-tempering treatment, resulting in a thermally induced martensite transformation into ferrite. Lyu et al. [106] also found that the soft δ-ferrite residue significantly affects the tensile properties and isotropy, as cracking starts at the interface or within the δ-ferrite due to the deformation incompatibility between the soft δ-ferrite and the hard martensitic matrix. Those findings are also consistent with those of Ge et al. [75], who studied the WAAM of H13. They measured a reduction in the hardness and tensile strength of the remelted overlap zone between two weld beads (martensite + ferrite) as compared to the single melted zone, which is almost entirely composed of martensite.

Furthermore, the intense precipitation along the interface between δ-ferrite and matrix may also contribute to the anisotropy. Consequently, the morphology, distribution, and proportion of detrimental δ-ferrite should be controlled to reduce the anisotropy and decrease tensile properties in martensitic AM structures [106]. Lyu et al. [106] had the morphology of δ-ferrite oriented and elongated along the build-up direction, i.e., perpendicular to the loading during a tensile test in a direction parallel (horizontal) to the welding direction. In the present study, the δ-ferrite was distributed predominantly homogeneously as a finely dispersed network, improving the isotropic conditions of the 3D printed material.

For the hot work tool steel grade X10CrMo6-3 and the welding sequence applied, the yield strength is about 1000–1100 MPa, and the ultimate tensile strength is about 1200–1400 MPa. However, limited information is available for the tensile properties of AM components made from carbon-bearing hot work tool steels (e.g. H13 [39,75]) produced by wire-based additive manufacturing. Therefore, properly comparing results remains challenging. The measured tensile strengths are comparatively higher and more consistent than for 2Cr13 [106,107] and H13 [39,75] martensitic grades produced by wire-based processes, but lower than for H11 and H13 grades produced by powder-based AM processes (Table 12) and wrought in the annealed condition (Fig. 19).

To achieve the desired mechanical properties for high temperature applications and to stabilize the microstructure for service conditions, hot work tool steels are usually subjected to tempering. The established heat treatment route for conventional hot work tool steel materials is austenitizing, quenching and double tempering, which usually leads to an improvement in the properties of hot work tool steels [109]. The martensitic matrix without precipitates obtained during quenching is hard and brittle, and tempering is used to regain some ductility by precipitating carbon in the form of carbides from the martensite matrix [80]. Since hardening during tempering is mainly due to the precipitation of secondary phases, the final microhardness is highly dependent on the volume fraction and size of the precipitates [109]. In AM, cooling rates are typically high during processing, and martensite formation is induced during AM processing of hot work tool steels [6,14]. The retained austenite of e.g. AISI H13 decomposes during post-heat treatment at 500 °C, and the cellular solidification structure disappears at tempering temperatures above 600–700 °C [7,8,80]. Full austenitization (1020 °C/70min) of AISI H13 followed by quenching and double tempering results in a tempered martensitic microstructure and carbides very similar to conventionally produced material [9].

In AM of carbon-bearing hot work tool steels (AISI H11/H13), the microstructure consists mainly of martensite and intercellular/interdendritic retained austenite. This contrasts with the present study and the material grades investigated, which contain a considerable amount of δ-ferrite and a negligible amount of retained austenite, compared to AM of AISI H11/H13. The transient as-built microstructure was inevitable because of the complex thermal history during the deposition process. Such a microstructure in turn would require additional or adapted heat treatments after AM [75]. To eliminate the undesirable heterogeneous δ-ferrite residues, a homogenization treatment followed by an established double tempering would provide a solution to homogenize the microstructure and restore mechanical properties. The homogenization treatment promotes dissolution of δ-ferrite and elemental redistribution into the austenitic matrix, which then transforms into martensite during subsequent cooling. Afshari et al. [110] and Ghaffari et al. [111] showed for WAAM of PH 13-8Mo that 1050 °C is sufficient to dissolve undesirable residual δ-ferrite phases, resulting in a fully martensitic microstructure. Rodrigues et al. [112] have shown for WAAM of 316L that changing the solution treatment from 1050 °C/2h to 1200 °C/1h can further reduce the residual δ-ferrite content from 2.8% to 0.5% (16.9% in the as-built state). A similar HT at 1200 °C/2h was sufficient in WAAM of P91 [84] to remove the heterogeneous

Table 11
Representative values for absorbed impact energy by Charpy V-notch testing at room temperature according to the literature for powder-based 3D printed AISI H13 hot work tool steel grade.

Process	Feed Stock	Material	Condition	Remark	Orientation	KJ [J]	Ref.
L-PBF	Powder	H13	As-Built		Vert.	5.4	[103]
			Annealed		Vert.	10.8	
L-PBF	Powder	H13	As-Built	Partially molten powder influences KJ	–	4–23	[104]
L-PBF	Powder	H13	As-Built	Build platform preheated 200 °C	–	6.0 ± 1.4	[105]
L-PBF	Powder	H13	As-Built	–	–	14.4	[102]

Table 12
Representative tensile strengths at room temperature according to the literature for powder and wire-based 3d printed AISI H11 and H13 hot work tool steel grades.

Process	Feed Stock	Material	Condition	Remark	Orientation	YS [MPa]	UTS [MPa]	Ref.
L-PBF	Powder	H11	As-Built		Hor.	–	~1000	[18]
					Vert.		2000–2100	
			Annealed		Hor.	–	1700–1800	
					Vert.		2148 ± 16	
L-PBF	Powder	H13	As-Built		Hor.	–	1150–1275	[99]
					Vert.	–	1550–1650	
LMD	Powder	H11	As-Built		Hor.	860 ± 8	1710 ± 170	[14]
			Tempered		Hor.	1630 ± 9	2130 ± 10	
			Annealed		Hor.	1480 ± 1	1800	
LMD	Powder	H13	As-Built		Hor.	1288 ± 54	1064 ± 51	[108]
					Vert.	1564 ± 24	2033 ± 38	
CMT	Wire	H13	As-Built	Martensite Zone	Hor.	–	1322	[75]
				Martensite + Ferrite Zone		–	847	
MIG	Wire	H13	As-Built	–	Hor.	.	1085	[39]
					Vert.	.	871	

microstructure (δ-ferrite, lath martensite, and MX precipitates) and form a single uniform martensite structure throughout the deposit. After homogenization and quenching, tempering can be performed for secondary hardening and to recover ductility.

Suitable post-processing heat treatments should be used to further stabilize and adapt the microstructure to ensure the required mechanical properties. The aforementioned post-processing heat treatments are the subject of future research to achieve the desired mechanical properties.

5. Conclusion

The present study successfully demonstrated wire-based additive manufacturing of hot work tool steel using various arc welding processes and energy input levels. Applying a proper interpass strategy and following a welding sequence, sound volumetric AM structures of a chromium-molybdenum hot work tool steel with a pre-defined structure were deposited on an AISI H11 substrate. The application of the CMT welding process resulted in higher weld beads than MAG, and the lower energy/heat input resulted in a faster build-up process for the same material input. In all cases, the AM parts exhibited good integrity and were subsequently characterized to determine their microstructural and mechanical properties. The results lead to the following conclusions:

- The AM structures exhibit similar microstructural features, regardless of the applied arc welding process and energy input used, when similar interlayer strategy is applied.
- The microstructure consists of an α/α′-matrix and a predominately finely distributed vermicular δ-ferrite network. Unlike in other carbon-bearing tool steels, no significant amount of retained austenite was measured. Intense precipitation of molybdenum-based precipitates with different morphology and composition was observed.
- The mechanical properties are comparable for all configurations, and the differences in the mean values of hardness, tensile strength, and absorbed impact energy are within standard deviation ranges.
- All specimens exhibited a relatively homogeneous hardness distribution across the entire cross-section. The average hardness values fall within the range of 380–390 HV1.
- The tensile strength of the AM deposits is 1000–1100 MPa yield strength and 1200–1400 MPa ultimate tensile strength, which corresponds to values for the tested heat-treated H11 substrate. These results are higher than the values reported in the literature for WAAM of a comparable AISI H13 grade.
- The absorbed impact energy at room temperature for the AM structures fabricated with a low material/energy input is 10–12 J, corresponding to 70–85% of the heat-treated H11 substrate.
- No significant differences in the tested mechanical properties (tensile strength, impact energy) of the horizontally and vertically oriented specimens were observed for all configurations, indicating that these properties are isotropic.

CRediT authorship contribution statement

Florian Pixner: Investigation, Methodology, Funding acquisition, Visualization, Writing – original draft, Writing – review & editing, Project administration. **Ricardo Buzolin:** Investigation, Validation, Visualization, Methodology, Writing – review & editing. **Fernando Warchomicka:** Investigation, Validation, Methodology, Writing – review & editing. **Mária Dománková:** Investigation, Validation, Writing – review & editing. **Mária Čaplovičová:** Investigation. **Florian Riedlsperger:** Investigation, Validation, Writing – review & editing. **Sebastian Fritsche:** Investigation. **Marta Orłowska:** Investigation, Validation, Writing – review & editing. **Josef Domitner:** Resources, Validation, Writing – review & editing. **Michael Lasnik:** Funding acquisition. **Norbert Enzinger:** Supervision, Validation, Funding acquisition, Writing – review & editing.

Declaration of competing interest

I declare no conflict of interests.

Data availability

Data will be made available on request.

Acknowledgments

This research was funded by the COMET programme within the K2 Center "Integrated Computational Material, Process and Product Engineering (IC-MPPE)" (Project No 859480). The Austrian Federal Ministries supported this programme for Transport, Innovation and Technology (BMVIT) and for Digital and Economic Affairs (BMDW), represented by the Austrian research funding association (FFG), and the federal provinces of Styria, Upper Austria, and Tyrol. RHB fis funded by the CD-Laboratory for Design of High-Performance Alloys by Thermomechanical Processing with the support of the Christian Doppler Society. FR gratefully acknowledges financial support from the FWF (P-31374). The authors thank Marko Puda for performing the welding experiments and Heinz Fasching for sample manufacturing. Open Access was funded by the Graz University of Technology.

Appendix A. Supplementary data

Supplementary data to this article can be found online at https://doi.org/10.1016/j.msea.2023.145799.

References

[1] E. Doege, B.-A. Behrens, Handbuch Umformtechnik, Springer, 2010.
[2] B. Buchmayr, Damage, lifetime, and repair of forging dies, BHM Berg- Hüttenmännische Monatsh. 162 (2017) 88–93, https://doi.org/10.1007/s00501-016-0566-3.
[3] R. Rahn, U. Schruff, Improved tool performance and cost control in the forging industry, in: Proceedings of the 8th International Tooling Conference, RWTH Aachen, 2009, pp. 2–4.
[4] J. Mayerhofer, S. Zinner, Innovative Stähle für Schmiedewerkzeuge - vom Anforderungsprofil zur erfolgreichen Anwendung, in: Proceedings of the Conference Schmiedewerkzeuge, 2011, pp. 117–135. Salzburg.
[5] F. Huber, C. Bischof, O. Hentschel, et al., Laser beam melting and heat-treatment of 1.2343 (AISI H11) tool steel – microstructure and mechanical properties, Mater. Sci. Eng., A 742 (2019) 109–115, https://doi.org/10.1016/j.msea.2018.11.001.
[6] R. Casati, M. Coduri, N. Lecis, et al., Microstructure and mechanical behavior of hot-work tool steels processed by Selective Laser Melting, Mater. Char. 137 (2018) 50–57, https://doi.org/10.1016/j.matchar.2018.01.015.
[7] J. Krell, A. Röttger, K. Geenen, W. Theisen, General investigations on processing tool steel X40CrMoV5-1 with selective laser melting, J. Mater. Process. Technol. 255 (2018) 679–688, https://doi.org/10.1016/j.jmatprotec.2018.01.012.
[8] F. Deirmina, N. Peghini, B. AlMangour, et al., Heat treatment and properties of a hot work tool steel fabricated by additive manufacturing, Mater. Sci. Eng., A 753 (2019) 109–121, https://doi.org/10.1016/j.msea.2019.03.027.
[9] M. Åsberg, G. Fredriksson, S. Hatami, et al., Influence of post treatment on microstructure, porosity and mechanical properties of additive manufactured H13 tool steel, Mater. Sci. Eng., A 742 (2019) 584–589, https://doi.org/10.1016/j.msea.2018.08.046.
[10] R. Dörfert, J. Zhang, B. Clausen, et al., Comparison of the fatigue strength between additively and conventionally fabricated tool steel 1.2344, Addit. Manuf. 27 (2019) 217–223, https://doi.org/10.1016/j.addma.2019.01.010.
[11] R. Mertens, B. Vrancken, N. Holmstock, et al., Influence of powder bed preheating on microstructure and mechanical properties of H13 tool steel SLM parts, Phys. Procedia 83 (2016) 882–890, https://doi.org/10.1016/j.phpro.2016.08.092.
[12] J. Šafka, M. Ackermann, L. Voleský, Structural properties of H13 tool steel parts produced with use of selective laser melting technology, J Phys Conf Ser 709 (2016), https://doi.org/10.1088/1742-6596/709/1/012004.
[13] O. Hentschel, L. Siegel, C. Scheitler, et al., Processing of AISI H11 tool steel powder modified with carbon black nanoparticles for the additive manufacturing of forging tools with tailored mechanical properties by means of laser metal deposition (LMD), Metals 8 (2018), https://doi.org/10.3390/met8090659.
[14] D. Junker, O. Hentschel, M. Schmidt, M. Merklein, Investigation of heat treatment strategies for additively-manufactured tools of X37CrMoV5-1, Metals 8 (2018) 854, https://doi.org/10.3390/met8100854.
[15] A. Bohlen, H. Freiße, M. Hunkel, F. Vollertsen, Additive manufacturing of tool steel by laser metal deposition, Procedia CIRP 74 (2018) 192–195, https://doi.org/10.1016/j.procir.2018.08.092.

[16] J. Choi, Y. Chang, Characteristics of laser aided direct metal/material deposition process for tool steel, Int. J. Mach. Tool Manufact. 45 (2005) 597–607, https://doi.org/10.1016/j.ijmachtools.2004.08.014.
[17] N.S. Bailey, C. Katinas, Y.C. Shin, Laser direct deposition of AISI H13 tool steel powder with numerical modeling of solid phase transformation, hardness, and residual stresses, J. Mater. Process. Technol. 247 (2017) 223–233, https://doi.org/10.1016/j.jmatprotec.2017.04.020.
[18] F. Huber, C. Bischof, O. Hentschel, et al., Laser beam melting and heat-treatment of 1.2343 (AISI H11) tool steel – microstructure and mechanical properties, Mater. Sci. Eng., A 742 (2019) 109–115, https://doi.org/10.1016/j.msea.2018.11.001.
[19] D. Ding, Z. Pan, D. Cuiuri, H. Li, Wire-feed additive manufacturing of metal components: technologies, developments and future interests, Int. J. Adv. Manuf. Technol. 81 (2015) 465–481, https://doi.org/10.1007/s00170-015-7077-3.
[20] voestalpine BÖHLER Edelstahl GmbH & Co KG, voestalpine BÖHLER Edelstahl - Schweissen im Werkzeugbau, 2010. https://www.bohler-edelstahl.com/app/uploads/sites/92/2020/02/productdb/api/bw140d_schweissen_im_werkzeugbau.pdf. (Accessed 10 January 2021).
[21] DSI-Laser DataSheet. https://www.dsi-laser.de/images/LaserMold60.TD.pdf.
[22] J. Stockinger, C. Wiednig, N. Enzinger, et al., Additive manufacturing via cold metal transfer, Met. Addit. Manuf. Conf. (2016) 117–125.
[23] F. Pixner, R. Buzolin, A. Zelić, et al., Tailoring the alloy composition for wire arc additive manufacturing utilizing metal-cored wires in the cold metal transfer process, Mater. Des. 215 (2022), 110453, https://doi.org/10.1016/j.matdes.2022.110453.
[24] D. Jafari, T.H.J. Vaneker, I. Gibson, Wire and arc additive manufacturing : opportunities and challenges to control the quality and accuracy of manufactured parts, Mater. Des. 202 (2021), 109471, https://doi.org/10.1016/j.matdes.2021.109471.
[25] J.S. Panchagnula, S. Simhambhatla, Robotics and Computer – Integrated Manufacturing Manufacture of Complex Thin-Walled Metallic Objects Using Weld-Deposition Based Additive Manufacturing, vol. 49, 2018, pp. 194–203, https://doi.org/10.1016/j.rcim.2017.06.003.
[26] J. Shi, F. Li, Effect of In-Process Active Cooling on Forming Quality and Efficiency of Tandem GMAW – Based Additive Manufacturing, 2019, pp. 1349–1356.
[27] P.M. Sequeira Almeida, S. Williams, Innovative process model of Ti-6Al-4V additive layer manufacturing using cold metal transfer (CMT), 21st Annu Int Solid Free Fabr Symp - An Addit. Manuf. Conf. SFF (2010) 25–36, 2010.
[28] Y. Ma, D. Cuiuri, N. Hoye, et al., The effect of location on the microstructure and mechanical properties of titanium aluminides produced by additive layer manufacturing using in-situ alloying and gas tungsten arc welding, Mater. Sci. Eng., A 631 (2015) 230–240, https://doi.org/10.1016/j.msea.2015.02.051.
[29] C. Shen, Z. Pan, D. Cuiuri, et al., Fabrication of Fe-FeAl functionally graded material using the wire-Arc Additive manufacturing process, Metall. Mater. Trans. B 47 (2016) 763–772, https://doi.org/10.1007/s11663-015-0509-5.
[30] C. Shen, Z. Pan, Y. Ma, et al., Fabrication of iron-rich Fe – Al intermetallics using the wire-arc additive manufacturing process, Addit. Manuf. 7 (2015) 20–26, https://doi.org/10.1016/j.addma.2015.06.001.
[31] H. Geng, J. Li, J. Xiong, et al., Optimization of wire feed for GTAW based additive manufacturing, J. Mater. Process. Technol. 243 (2017) 40–47, https://doi.org/10.1016/j.jmatprotec.2016.11.027.
[32] W. Aiyiti, W. Zhao, B. Lu, Y. Tang, Investigation of the overlapping parameters of MPAW-based rapid prototyping, Rapid Prototyp. J. 12 (2006) 165–172, https://doi.org/10.1108/13552540610670744.
[33] H. Zhang, J. Xu, G. Wang, Fundamental Study on Plasma Deposition Manufacturing, vol. 171, 2003, pp. 112–118, https://doi.org/10.1016/S0257-8972(03)00250-0.
[34] F. Martina, J. Mehnen, S.W. Williams, et al., Investigation of the benefits of plasma deposition for the additive layer manufacture of Ti-6Al-4V, J. Mater. Process. Technol. 212 (2012) 1377–1386, https://doi.org/10.1016/j.jmatprotec.2012.02.002.
[35] F. Matos, F. Ribeiro, L. João, et al., Thermal management in WAAM through the CMT Advanced process and an active cooling technique, J. Manuf. Process. 57 (2020) 23–35, https://doi.org/10.1016/j.jmapro.2020.06.007.
[36] L. João, D.M. Souza, DB De Araújo, et al., Concept and Validation of an Active Cooling Technique to Mitigate Heat Accumulation in WAAM, 2020, pp. 2513–2523.
[37] T.A. Rodrigues, V. Duarte, J.A. Avila, et al., Wire and arc additive manufacturing of HSLA steel: effect of thermal cycles on microstructure and mechanical properties, Addit. Manuf. 27 (2019) 440–450, https://doi.org/10.1016/j.addma.2019.03.029.
[38] Y. Ali, P. Henckell, J. Hildebrand, et al., Wire arc additive manufacturing of hot work tool steel with CMT process, J. Mater. Process. Technol. 269 (2019) 109–116, https://doi.org/10.1016/j.jmatprotec.2019.01.034.
[39] T. Wang, Y. Zhang, Z. Wu, C. Shi, Microstructure and properties of die steel fabricated by WAAM using, Vaccum 149 (2018) 185–189, https://doi.org/10.1016/j.vacuum.2017.12.034.
[40] Y.M. Zhang, P. Li, Y. Chen, A.T. Male, Automated System for Welding-Based Rapid Prototyping, vol. 12, 2002, pp. 37–53.
[41] G. Posch, K. Chladil, H. Chladil, Material properties of CMT—metal additive manufactured duplex stainless steel blade-like geometries, Weld. World 61 (2017) 873–882, https://doi.org/10.1007/s40194-017-0474-5.
[42] J. Ding, P. Colegrove, J. Mehnen, et al., Thermo-mechanical analysis of wire and Arc Additive layer manufacturing process on large multi-layer parts, Comput. Mater. Sci. 50 (2011) 3315–3322, https://doi.org/10.1016/j.commatsci.2011.06.023.
[43] Fronius CMT – COLD METAL TRANSFER: THE COLD WELDING PROCESS FOR PREMIUM QUALITY. https://www.fronius.com/en/welding-technology/world-of-welding/fronius-welding-processes/cmt.
[44] H.T. Zhang, J.C. Feng, P. He, et al., The Arc Characteristics and Metal Transfer Behaviour of Cold Metal Transfer and its Use in Joining Aluminium to Zinc-Coated Steel, vol. 499, 2009, pp. 111–113, https://doi.org/10.1016/j.msea.2007.11.124.
[45] C.G. Pickin, S.W. Williams, M. Lunt, Journal of Materials Processing Technology Characterisation of the cold metal transfer (CMT) process and its application for low dilution cladding, J. Mater. Process. Technol. 211 (2011) 496–502, https://doi.org/10.1016/j.jmatprotec.2010.11.005.
[46] J. Plangger, P. Schabhüttl, T. Vuherer, N. Enzinger, Cmt additive manufacturing of a high strength steel alloy for application in crane construction, Metals 9 (2019) 1–14, https://doi.org/10.3390/met9060650.
[47] P. Gerhard, K. Ferdinand, C. Harald, Manufacturing of turbine blades by shape giving CMT Welding, Met. Addit. Manuf. Conf. 10 (2014).
[48] J. Gu, J. Ding, S.W. Williams, et al., The effect of inter-layer cold working and post-deposition heat treatment on porosity in additively manufactured aluminum alloys, J. Mater. Process. Technol. 230 (2016) 26–34, https://doi.org/10.1016/j.jmatprotec.2015.11.006.
[49] S.H. Lee, CMT-based wire arc additive manufacturing using 316l stainless steel: effect of heat accumulation on the multi-layer deposits, Metals 10 (2020), https://doi.org/10.3390/met10020278.
[50] L. Vázquez, N. Rodríguez, I. Rodríguez, et al., Influence of interpass cooling conditions on microstructure and tensile properties of Ti-6Al-4V parts manufactured by WAAM, Weld. World 64 (2020) 1377–1388, https://doi.org/10.1007/s40194-020-00921-3.
[51] O. Panchenko, D. Kurushkin, F. Isupov, et al., Gas Metal Arc Welding Modes in Wire Arc Additive Manufacturing of Ti-6Al-4V, 2021.
[52] R.M. Kindermann, M.J. Roy, R. Morana, P.B. Prangnell, Process response of Inconel 718 to wire + arc additive manufacturing with cold metal transfer, Mater. Des. 195 (2020), 109031, https://doi.org/10.1016/j.matdes.2020.109031.
[53] W. Yangfan, C. Xizhang, S. Chuanchu, Microstructure and mechanical properties of Inconel 625 fabricated by wire-arc additive manufacturing, Surf. Coating. Technol. 374 (2019) 116–123, https://doi.org/10.1016/j.surfcoat.2019.05.079.
[54] A.N.M. Tanvir, M.R.U. Ahsan, C. Ji, et al., Heat treatment effects on Inconel 625 components fabricated by wire + arc additive manufacturing (WAAM)—part 1: microstructural characterization, Int. J. Adv. Manuf. Technol. (2019) 3785–3798, https://doi.org/10.1007/s00170-019-03828-6.
[55] T. Klein, A. Arnoldt, M. Schnall, S. Gneiger, Microstructure Formation and mechanical properties of a wire-Arc Additive manufactured magnesium alloy, JOM 73 (2021) 1126–1134, https://doi.org/10.1007/s11837-021-04567-4.
[56] S. Gneiger, J.A. Österreicher, A.R. Arnoldt, et al., Development of a High Strength Magnesium Alloy for Wire Arc Additive Manufacturing, 2020 m.
[57] P. Wang, H. Zhang, H. Zhu, et al., Wire-arc additive manufacturing of AZ31 magnesium alloy fabricated by cold metal transfer heat source : processing , microstructure , and mechanical behavior, J. Mater. Process. Technol. 288 (2021), 116895, https://doi.org/10.1016/j.jmatprotec.2020.116895.
[58] T. Klein, M. Schnall, Control of macro-/microstructure and mechanical properties of a wire-arc additive manufactured aluminum alloy, Int. J. Adv. Manuf. Technol. 108 (2020) 235–244, https://doi.org/10.1007/s00170-020-05396-6.
[59] T. Klein, M. Schnall, B. Gomes, et al., Wire-arc additive manufacturing of a novel high-performance Al-Zn-Mg-Cu alloy : processing , characterization and feasibility demonstration, Addit. Manuf. 37 (2021), 101663, https://doi.org/10.1016/j.addma.2020.101663.
[60] Voestalpine Böhler Welding UTP Maintenance A 73 G 4 Datasheet. http://www.vabw-service.com/documents/utp/datenblaetter/de/UTP A 73 G 4.pdf?cache=1547041611. Accessed 24 November 2022.
[61] voestalpine BÖHLER Edelstahl GmbH & Co KG AISI H11 ISOBLOCK W300 Datasheet. https://www.bohler-edelstahl.com/de/products/w300isobloc/. Accessed 24 November 2022.
[62] S. Zhang, Q. Wang, R. Yang, C. Dong, Composition equivalents of stainless steels understood via gamma stabilizing efficiency, Sci. Rep. 11 (2021) 5423, https://doi.org/10.1038/s41598-021-84917-z.
[63] Y. Cao, S. Zhu, X. Liang, W. Wang, Overlapping model of beads and curve fitting of bead section for rapid manufacturing by robotic MAG welding process, Robot. Comput. Integrated Manuf. 27 (2011) 641–645, https://doi.org/10.1016/j.rcim.2010.11.002.
[64] F. Pixner, F. Warchomicka, P. Peter, et al., Wire-based additive manufacturing of Ti-6Al-4V using electron beam technique, Materials 13 (2020) 3310, https://doi.org/10.3390/ma13153310.
[65] J. Xiong, G. Zhang, H. Gao, L. Wu, Modeling of bead section profile and overlapping beads with experimental validation for robotic GMAW-based rapid manufacturing, Robot. Comput. Integrated Manuf. 29 (2013) 417–423, https://doi.org/10.1016/j.rcim.2012.09.011.
[66] D.G. Brandon, The structure of high-angle grain boundaries, Acta Metall. 14 (1966) 1479–1484, https://doi.org/10.1016/0001-6160(66)90168-4.
[67] L. Onsager, Reciprocal relations in irreversible processes. I, Phys. Rev. 37 (1931) 405–426, https://doi.org/10.1103/PhysRev.37.405.
[68] A.S. Oliveira, RO Dos Santos, B.C. Silva, S. dos, et al., A detailed forecast of the technologies based on lifecycle analysis of GMAW and CMT welding processes, Sustainability 13 (2021) 3766, https://doi.org/10.3390/su13073766.
[69] D. Galeazzi, RHG.e. Silva, A.B. Viviani, et al., Evaluation of thermal and geometric properties of martensitic stainless steel thin walls built by additive

manufacturing cold metal transfer (CMT) processes, Int. J. Adv. Manuf. Technol. 120 (2022) 2151–2165, https://doi.org/10.1007/s00170-022-08921-x.
[70] B.P. Nagasai, S. Malarvizhi, V. Balasubramanian, Mechanical properties and microstructural characteristics of wire arc additive manufactured 308 L stainless steel cylindrical components made by gas metal arc and cold metal transfer arc welding processes, J. Mater. Process. Technol. 307 (2022), 117655, https://doi.org/10.1016/j.jmatprotec.2022.117655.
[71] J.L. Prado-Cerqueira, A.M. Camacho, J.L. Diéguez, et al., Analysis of favorable process conditions for the manufacturing of thin-wall pieces of mild steel obtained by wire and arc additive manufacturing (WAAM), Materials 11 (2018), https://doi.org/10.3390/ma11081449.
[72] K.S. Derekar, A. Addison, S.S. Joshi, et al., Effect of pulsed metal inert gas (pulsed-MIG) and cold metal transfer (CMT) techniques on hydrogen dissolution in wire arc additive manufacturing (WAAM) of aluminium, Int. J. Adv. Manuf. Technol. 107 (2020) 311–331, https://doi.org/10.1007/s00170-020-04946-2.
[73] J. Feng, H. Zhang, P. He, The CMT short-circuiting metal transfer process and its use in thin aluminium sheets welding, Mater. Des. 30 (2009) 1850–1852, https://doi.org/10.1016/j.matdes.2008.07.015.
[74] Voestalpine Böhler Welding, Filler Metals for Repair, Hardfacing and Cladding Applications, 2013, p. 512.
[75] J. Ge, T. Ma, Y. Chen, et al., Wire-arc additive manufacturing H13 part: 3D pore distribution, microstructural evolution, and mechanical performances, J. Alloys Compd. 783 (2019) 145–155, https://doi.org/10.1016/j.jallcom.2018.12.274.
[76] J. Gu, J. Ding, S.W. Williams, et al., The strengthening effect of inter-layer cold working and post-deposition heat treatment on the additively manufactured Al-6.3Cu alloy, Mater. Sci. Eng., A 651 (2016) 18–26, https://doi.org/10.1016/j.msea.2015.10.101.
[77] F. Montevecchi, G. Venturini, N. Grossi, et al., Idle time selection for wire-arc additive manufacturing: a finite element-based technique, Addit. Manuf. 21 (2018) 479–486, https://doi.org/10.1016/j.addma.2018.01.007.
[78] S. Amirabdollahian, F. Deirmina, M. Pellizzari, et al., Tempering behavior of a direct laser deposited hot work tool steel: influence of quenching on secondary hardening and microstructure, Mater. Sci. Eng., A 814 (2021), 141126, https://doi.org/10.1016/j.msea.2021.141126.
[79] W. Wu, L.Y. Hwu, D.Y. Lin, J.L. Lee, The relationship between alloying elements and retained austenite in martensitic stainless steel welds, Scripta Mater. 42 (2000) 1071–1076, https://doi.org/10.1016/S1359-6462(00)00339-0.
[80] P. Bajaj, A. Hariharan, A. Kini, et al., Steels in additive manufacturing: a review of their microstructure and properties, Mater. Sci. Eng., A 772 (2020), 138633, https://doi.org/10.1016/j.msea.2019.138633.
[81] J. Lunde, M. Kazemipour, S. Salahi, A. Nasiri, Wire Arc additive manufacturing of AISI 420 martensitic stainless steel: on as-printed microstructure and mechanical properties, J. Mater. Eng. Perform. 30 (2021) 9181–9191, https://doi.org/10.1007/s11665-021-06118-z.
[82] E.B. Fonseca, J.D. Escobar, A.H.G. Gabriel, et al., Tempering of an additively manufactured microsegregated hot-work tool steel: a high-temperature synchrotron X-ray diffraction study, Addit. Manuf. 55 (2022), 102812, https://doi.org/10.1016/j.addma.2022.102812.
[83] F. Deirmina, P.A. Davies, N. Dixit, et al., Production and characterization of a modified hot work tool steel by laser powder bed fusion, Metall. Mater. Trans. A 53 (2022) 2642–2651, https://doi.org/10.1007/s11661-022-06694-2.
[84] K. Li, M.A. Klecka, S. Chen, W. Xiong, Wire-arc additive manufacturing and post-heat treatment optimization on microstructure and mechanical properties of Grade 91 steel, Addit. Manuf. 37 (2021), 101734, https://doi.org/10.1016/j.addma.2020.101734.
[85] M. Ghaffari, A. Vahedi Nemani, A. Nasiri, Microstructure and mechanical behavior of PH 13–8Mo martensitic stainless steel fabricated by wire arc additive manufacturing, Addit. Manuf. 49 (2022), 102374, https://doi.org/10.1016/j.addma.2021.102374.
[86] S. Salahi, A.V. Nemani, M. Ghaffari, et al., On microstructure, crystallographic orientation, and corrosion properties of wire arc additive manufactured 420 martensitic stainless steel: effect of the inter-layer temperature, Addit. Manuf. 46 (2021), 102157, https://doi.org/10.1016/j.addma.2021.102157.
[87] C.Y. Chou, N.H. Pettersson, A. Durga, et al., Influence of solidification structure on austenite to martensite transformation in additively manufactured hot-work tool steels, Acta Mater. 215 (2021), 117044, https://doi.org/10.1016/j.actamat.2021.117044.
[88] C. Lerchbacher, The Effect of Cooling Rate on the Microstructure and its Influence on Toughness of Two Types of Tool Steels Studied by High Resolution Techniques, 2013.
[89] M.V. Upadhyay, M.B.H. Slama, S. Gaudez, et al., Non-oxide precipitates in additively manufactured austenitic stainless steel, Sci. Rep. 11 (2021) 1–18, https://doi.org/10.1038/s41598-021-89873-2.
[90] T. Chen, S. Xue, B. Wang, et al., Study on short-circuiting GMAW pool behavior and microstructure of the weld with different waveform control methods, Metals 9 (2019), https://doi.org/10.3390/met9121326.
[91] X. Lou, P.L. Andresen, R.B. Rebak, Oxide inclusions in laser additive manufactured stainless steel and their effects on impact toughness and stress corrosion cracking behavior, J. Nucl. Mater. 499 (2018) 182–190, https://doi.org/10.1016/j.jnucmat.2017.11.036.
[92] P. Deng, M. Karadge, R.B. Rebak, et al., The origin and formation of oxygen inclusions in austenitic stainless steels manufactured by laser powder bed fusion, Addit. Manuf. 35 (2020), 101334, https://doi.org/10.1016/j.addma.2020.101334.
[93] M. Song, X. Lin, F. Liu, et al., Effect of environmental oxygen content on the oxide inclusion in laser solid formed AISI 420 stainless steel, Mater. Des. 90 (2016) 459–467, https://doi.org/10.1016/j.matdes.2015.11.003.
[94] X. Yang, F. Tang, X. Hao, Z. Li, Oxide evolution during the solidification of 316L stainless steel from additive manufacturing powders with different oxygen contents, Metall. Mater. Trans. B Process Metall. Mater. Process. Sci. 52 (2021) 2253–2262, https://doi.org/10.1007/s11663-021-02191-w.
[95] Da Costa E Silva ALV, The effects of non-metallic inclusions on properties relevant to the performance of steel in structural and mechanical applications, J. Mater. Res. Technol. 8 (2019) 2408–2422, https://doi.org/10.1016/j.jmrt.2019.01.009.
[96] W.H. Cubberly, Tool and Manufacturing Engineers Handbook Desk Edition, 1989.
[97] J.M. Beswick, Bearing Steel Technology, 2002.
[98] A. Fischer, K. Bobzin, Friction, Wear and Wear Protection, 2008.
[99] M.J. Holzweissig, A. Taube, F. Brenne, et al., Microstructural characterization and mechanical performance of hot work tool steel processed by selective laser melting, Metall. Mater. Trans. B Process Metall. Mater. Process. Sci. 46 (2015) 545–549, https://doi.org/10.1007/s11663-014-0267-9.
[100] S.H. Oliari, A.S.C.M. D'Oliveira, M. Schulz, Additive manufacturing of H11 with wire-based laser metal deposition, Soldag Inspeção 22 (2017) 466–479, https://doi.org/10.1590/0104-9224/si2204.06.
[101] M. Teli, F. Klocke, K. Arntz, et al., Study for combined wire + powder laser metal deposition of H11 and niobium, Procedia Manuf. 25 (2018) 426–434, https://doi.org/10.1016/j.promfg.2018.06.113.
[102] B. Ren, D. Lu, R. Zhou, et al., Preparation and mechanical properties of selective laser melted H13 steel, J. Mater. Res. 34 (2019) 1415–1425, https://doi.org/10.1557/jmr.2019.10.
[103] M. Ackermann, J. Šafka, L. Voleský, et al., Impact testing of H13 tool steel processed with use of selective laser melting technology, Mater. Sci. Forum 919 (2018) 43–51. https://doi.org/10.4028/www.scientific.net/MSF.919.43.
[104] Wu L Full Paper MAMC2018 - Xia.
[105] L. Wu, F. Xia, W. Gridin, et al., Laser beam melting of H13 tool steel: from the evolution of microstructure to process simulation, Euro PM (2020), https://doi.org/10.2139/ssrn.3860221, 2018 Congr Exhib 2–7.
[106] Z. Lyu, Y.S. Sato, S. Tokita, et al., Microstructural distribution and anisotropic tensile behavior in a 2Cr13 martensitic stainless steel thin wall fabricated by wire arc additive manufacturing, Mater. Today Commun. 29 (2021), 102870, https://doi.org/10.1016/j.mtcomm.2021.102870.
[107] J. Ge, J. Lin, Y. Chen, et al., Characterization of wire arc additive manufacturing 2Cr13 part: process stability, microstructural evolution, and tensile properties, J. Alloys Compd. 748 (2018) 911–921, https://doi.org/10.1016/j.jallcom.2018.03.222.
[108] L. Xue, J. Chen, S.H. Wang, Freeform laser consolidated H13 and CPM 9V tool steels, Metallogr Microstruct Anal 2 (2013) 67–78, https://doi.org/10.1007/s13632-013-0061-0.
[109] M. Laleh, E. Sadeghi, R.I. Revilla, et al., Heat treatment for metal additive manufacturing, Prog. Mater. Sci. 133 (2023), 101051, https://doi.org/10.1016/j.pmatsci.2022.101051.
[110] E. Afshari, M. Ghaffari, A. Vahedi Nemani, A. Nasiri, Effect of heat treatment on microstructure and tribological performance of PH 13-8Mo stainless steel fabricated via wire arc additive manufacturing, Wear (2023), 204947, https://doi.org/10.1016/j.wear.2023.204947, 526–527.
[111] M. Ghaffari, A. Vahedi Nemani, A. Nasiri, Microstructural evolution and mechanical performance after precipitation hardening of PH 13-8Mo martensitic stainless steel fabricated by wire arc additive manufacturing, Materialia 24 (2022), 101507, https://doi.org/10.1016/j.mtla.2022.101507.
[112] T.A. Rodrigues, J.D. Escobar, J. Shen, et al., Effect of heat treatments on 316 stainless steel parts fabricated by wire and arc additive manufacturing: microstructure and synchrotron X-ray diffraction analysis, Addit. Manuf. 48 (2021), 102428, https://doi.org/10.1016/j.addma.2021.102428.